*J. Fluid Mech.* (2018), *vol.* 854, *pp.* 293–323. © Cambridge University Press 2018
doi:10.1017/jfm.2018.641



# Strato-hyperbolic instability: a new mechanism of instability in stably stratified vortices

**Shota Suzuki**[1], **Makoto Hirota**[2] **and Yuji Hattori**[2,†]

[1]Graduate School of Information Sciences, Tohoku University, Sendai 980-8579, Japan

[2]Institute of Fluid Science, Tohoku University, Sendai 980–8577, Japan

(Received 24 November 2017; revised 27 April 2018; accepted 2 August 2018;
first published online 6 September 2018)

The stability of stably stratified vortices is studied by local stability analysis. Three base flows that possess hyperbolic stagnation points are considered: the two-dimensional (2-D) Taylor–Green vortices, the Stuart vortices and the Lamb–Chaplygin dipole. It is shown that the elliptic instability is stabilized by stratification; it is completely stabilized for the 2-D Taylor–Green vortices, while it remains and merges into hyperbolic instability near the boundary or the heteroclinic streamlines connecting the hyperbolic stagnation points for the Stuart vortices and the Lamb–Chaplygin dipole. More importantly, a new instability caused by hyperbolic instability near the hyperbolic stagnation points and phase shift by the internal gravity waves is found; it is named the strato-hyperbolic instability; the underlying mechanism is parametric resonance as unstable band structures appear in contours of the growth rate. A simplified model explains the mechanism and the resonance curves. The growth rate of the strato-hyperbolic instability is comparable to that of the elliptic instability for the 2-D Taylor–Green vortices, while it is smaller for the Stuart vortices and the Lamb–Chaplygin dipole. For the Lamb–Chaplygin dipole, the tripolar instability is found to merge with the strato-hyperbolic instability as stratification becomes strong. The modal stability analysis is also performed for the 2-D Taylor–Green vortices. It is shown that global modes of the strato-hyperbolic instability exist; the structure of an unstable eigenmode is in good agreement with the results obtained by local stability analysis. The strato-hyperbolic mode becomes dominant depending on the parameter values.

**Key words:** parametric instability, stratified flows, vortex instability

## 1. Introduction

Vortices are frequently encountered in atmospheric and oceanographic fluids not only on Earth but also on other planets like Jupiter. They are under the effects of density stratification due to gravity and planetary rotation. Many efforts have been devoted to fully understand the dynamics of vortices in stratified fluids since it is indispensable for understanding and predicting the creation and evolution of strong vortices like hurricanes on Earth and the Great Red Spot on Jupiter.

† Email address for correspondence: hattori@fmail.ifs.tohoku.ac.jp

In this paper, we show, mostly by local stability analysis, that there exists a new short-wave instability in stably stratified vortices, while modal stability analysis is also performed to confirm it. This instability is caused by hyperbolic instability near the hyperbolic stagnation points and phase shift by inertial gravity waves; hence, there should be hyperbolic stagnation points in the flow, which usually exist when there are multiple vortices. Therefore, this new instability is expected to occur generally in stratified fluids. The effects of stratification on the elliptic instability are also investigated.

Stability is one of the fundamental properties of stratified vortices that form a basis for understanding their dynamics. Many efforts have been devoted to exploring the stability of stratified vortices. The effects of stratification on the stability of columnar vortices in the $f$-plane or rotating fluids were studied by Potylitsin & Peltier (1998), who focused on the role of the centrifugal instability. The zigzag instability has been studied by several authors since Billant & Chomaz (2000*a*) found by experiments that it occurs for a vertical columnar vortex pair and clarified its mechanism theoretically (Billant & Chomaz 2000*b*) and numerically (Billant & Chomaz 2000*c*). It can lead to breakdown of vortices (Waite & Smolarkiewicz 2008). It has been shown to occur also in co-rotating vortices in stratified fluids (Otheguy, Billant & Chomaz 2006*a*,*b*) and vortex pairs in stratified and rotating fluids (Billant 2010; Billant *et al.* 2010). It is essentially a long-wave instability for which the wavelength is much larger than the size of the vortex cores, although the wavelength can be short for strong stratification; it should be noted that it does not deform the vortex cores very much, while the centrelines of the vortices are deformed in a zigzag shape. Caulfield & Peltier (2000) showed that Kelvin–Helmholtz (KH) billows that develop in stratified free shear layers are subject to three-dimensional secondary instabilities; but the vorticity of the KH billows are perpendicular to the direction of gravity, which is different from the studies above and the present study (see also Itano 2004).

Unfortunately, on the other hand, the short-wave instability for which the wavelength is shorter than or of the same order as the vortex cores has not been sufficiently explored. For homogeneous (non-stratified) fluids, the hyperbolic instability and the elliptic instability are known to occur. The hyperbolic instability occurs in the vicinity of hyperbolic stagnation points. It was shown analytically by local stability analysis (Friedlander & Vishik 1991; Lifschitz & Hameiri 1991) and for a linear hyperbolic flow (Caulfield & Kerswell 2000). Linear and nonlinear evolution of the hyperbolic instability in two-dimensional (2-D) Taylor–Green vortices was studied by Leblanc & Godeferd (1999). The role of hyperbolic instability has been discussed for mixing layers (Caulfield & Kerswell 2000; Arratia, Caulfield & Chomaz 2013) and flow past a cylinder (Leweke & Williamson 1998*b*; Pralits, Giannetti & Brandt 2013). For stratified fluids, however, there is no work on the hyperbolic instability except that of Caulfield & Peltier (2000), who showed that the hyperbolic instability is insignificant in the secondary instability of strongly stratified free shear layers. The elliptic instability occurs in homogeneous flows having elliptical streamlines and has been studied extensively since Moore & Saffman (1975) and Tsai & Widnall (1976) showed analytically that a line vortex in a strain field is unstable to three-dimensional disturbances. The essential mechanism was revealed numerically by Pierrehumbert (1986) and analytically by Bayly (1986) and Waleffe (1990). It has been studied also by experiments (Malkus 1989; Leweke & Williamson 1998*a*; Eloy, Le Gal & Le Dizès 2000; Meunier & Leweke 2005). See Kerswell (2002) for a review. In contrast, there have been a limited number of results on the elliptic instability of stratified vortices (Miyazaki & Fukumoto 1992; Miyazaki & Adachi 1998; Otheguy

*et al.* 2006*a*; Guimbard *et al.* 2010). One of the reasons for this may be that the elliptic instability has been shown to be stabilized by stratification (Miyazaki & Fukumoto 1992; Billant & Chomaz 2000*b*). However, other short-wave instabilities, if they exist, can be important, directly giving rise to small-scale turbulence since the Reynolds number is usually high in atmospheric and oceanographic fluids so that they are hardly damped by viscous diffusion; it should be pointed out that the zigzag instability requires transition after nonlinear evolution to excite small-scale turbulence (Deloncle, Billant & Chomaz 2008).

This paper is organized as follows. In § 2 we briefly summarize the local stability analysis of stratified vortices; some useful formulations are also introduced. In § 3 we study the stability of the stably stratified 2-D Taylor–Green vortices; a new instability is found and its mechanism is clarified using a simplified model. Two other base flows are studied in § 4 in order to show the universality of the new instability. In § 5 the modal stability analysis of the 2-D Taylor–Green vortices is performed to confirm that the new instability appears as global modes. We conclude in § 6.

## 2. Local stability analysis of stratified vortices

### 2.1. *Local stability analysis*

We briefly summarize the derivation of the equations used in the local stability analysis (Friedlander & Vishik 1991; Lifschitz & Hameiri 1991). We consider the linear stability of a stably stratified inviscid flow under the Boussinesq approximation. The base flow is assumed steady. The velocity, pressure and density field are decomposed as

$$\boldsymbol{u} = \boldsymbol{u}_b + \boldsymbol{u}', \tag{2.1}$$

$$p = p_b + p', \tag{2.2}$$

$$\rho = \rho_0 + \alpha x_3 + \rho', \tag{2.3}$$

where $(\boldsymbol{u}_b, p_b, \rho_b = \rho_0 + \alpha x_3)$ and $(\boldsymbol{u}', p', \rho')$ are the base flow and the disturbance, the direction of the gravity force is taken as $-\boldsymbol{e}_3$ and $\alpha = \partial\rho_b/\partial x_3 < 0$ is a constant. The magnitude of the disturbance is infinitesimally small. The governing equations of the disturbance read

$$\boldsymbol{\nabla}\cdot\boldsymbol{u}' = 0, \tag{2.4}$$

$$\frac{\partial \boldsymbol{u}'}{\partial t} + (\boldsymbol{u}'\cdot\boldsymbol{\nabla})\boldsymbol{u}_b + (\boldsymbol{u}_b\cdot\boldsymbol{\nabla})\boldsymbol{u}' = -\frac{1}{\rho_0}\boldsymbol{\nabla}p' - g\frac{\rho'}{\rho_0}\boldsymbol{e}_3, \tag{2.5}$$

$$\frac{\partial \rho'}{\partial t} + (\boldsymbol{u}_b\cdot\boldsymbol{\nabla})\rho' + \alpha u_3' = 0, \tag{2.6}$$

where $g$ is the acceleration due to gravity. Note that diffusion of density is neglected. Let $U_0$ and $L_0$ be a characteristic velocity and a length scale. We rescale the velocity by $U_0$, the length by $L_0$, the pressure by $\rho_0 U_0^2$ and the density by $\rho_0 U_0^2/(gL_0)$; in contrast to Billant & Chomaz (2000*a*) the horizontal and vertical length scales are assumed to be of the same order of magnitude. Then the equations above are non-dimensionalized as

$$\boldsymbol{\nabla}\cdot\boldsymbol{u}' = 0, \tag{2.7}$$

$$\frac{\partial \boldsymbol{u}'}{\partial t} + (\boldsymbol{u}'\cdot\boldsymbol{\nabla})\boldsymbol{u}_b + (\boldsymbol{u}_b\cdot\boldsymbol{\nabla})\boldsymbol{u}' = -\boldsymbol{\nabla}p' - \rho'\boldsymbol{e}_3, \tag{2.8}$$

$$\frac{\partial \rho'}{\partial t} + (\boldsymbol{u}_b \cdot \boldsymbol{\nabla})\rho' - \frac{1}{F_h^2} u_3' = 0, \tag{2.9}$$

where $F_h = U_0/(L_0 N)$ is the Froude number and $N = \sqrt{-\alpha g/\rho_0}$ is the Brunt–Väisälä frequency.

In the local stability analysis the disturbance is assumed to be in the form of a wave packet,

$$\boldsymbol{u}' = (\hat{\boldsymbol{u}}_0 + \delta \hat{\boldsymbol{u}}_1 + \cdots) \exp\left(\frac{\mathrm{i}}{\delta}\Phi\right), \tag{2.10}$$

$$p' = (\hat{p}_0 + \delta \hat{p}_1 + \cdots) \exp\left(\frac{\mathrm{i}}{\delta}\Phi\right), \tag{2.11}$$

$$\rho' = (\hat{\rho}_0 + \delta \hat{\rho}_1 + \cdots) \exp\left(\frac{\mathrm{i}}{\delta}\Phi\right), \tag{2.12}$$

where $\delta$ is a small parameter and $\Phi$ is the eikonal satisfying $\mathrm{D}\Phi/\mathrm{D}t = 0$ ($\mathrm{D}/\mathrm{D}t = \partial/\partial t + \boldsymbol{u}_b \cdot \boldsymbol{\nabla}$). Substituting the above expressions into (2.7)–(2.9) yields a set of ordinary differential equations at the leading order

$$\boldsymbol{a} \cdot \boldsymbol{k} = 0, \tag{2.13}$$

$$\frac{\mathrm{d}\boldsymbol{x}}{\mathrm{d}t} = \boldsymbol{u}_b, \tag{2.14}$$

$$\frac{\mathrm{d}\boldsymbol{k}}{\mathrm{d}t} = -\boldsymbol{L}^{\mathrm{T}}\boldsymbol{k}, \tag{2.15}$$

$$\frac{\mathrm{d}\boldsymbol{a}}{\mathrm{d}t} = \left(2\frac{\boldsymbol{k}\boldsymbol{k}^{\mathrm{T}}}{|\boldsymbol{k}|^2} - \boldsymbol{I}\right)\boldsymbol{L}\boldsymbol{a} + \left(\frac{\boldsymbol{k}\boldsymbol{k}^{\mathrm{T}}}{|\boldsymbol{k}|^2} - \boldsymbol{I}\right) r\boldsymbol{e}_3, \tag{2.16}$$

$$\frac{\mathrm{d}r}{\mathrm{d}t} = \frac{1}{F_h^2} a_3, \tag{2.17}$$

where $\boldsymbol{k} = \boldsymbol{\nabla}\Phi$, $\boldsymbol{a} = \hat{\boldsymbol{u}}_0$, $r = \hat{\rho}_0$, $L_{ij} = \partial u_{b,i}/\partial x_j$ and $\boldsymbol{I}$ is the identity matrix (Friedlander & Vishik 1991); it is pointed out that pressure is eliminated using the incompressibility condition. If there exist initial conditions for which the amplitude of the disturbances $\boldsymbol{a}$ and $r$ grows unboundedly, the base flow is unstable.

We consider periodic orbits of fluid particles throughout this paper except in § 4.1 where this condition is slightly relaxed. We also assume that the wavevector $\boldsymbol{k}$ be time-periodic, which is a necessary condition for exponential instability of periodic orbits. It is known that $\boldsymbol{k}$ is time-periodic if it is perpendicular to the streamline initially,

$$\boldsymbol{k}(0) \cdot \boldsymbol{u}_b(\boldsymbol{x}(0)) = 0. \tag{2.18}$$

Then the time evolution of amplitude is described by a Floquet matrix $\boldsymbol{F}$ since the matrices which appear in (2.16) are also time-periodic:

$$\{\boldsymbol{a}, r\}(t+T) = \boldsymbol{F}(T)\{\boldsymbol{a}, r\}(t), \tag{2.19}$$

where $T$ is the period of $\boldsymbol{k}$ which coincides with that of the particle motion $\boldsymbol{x}$. Our task is to calculate the eigenvalues $\{\mu_i\}$ of $\boldsymbol{F}(T)$ which determine the growth rate as

$$\sigma_i = \frac{\log|\mu_i|}{T}. \tag{2.20}$$

### 2.2. *Numerical procedure*

In this paper we consider two-dimensional base flows which do not depend on $x_3$: $\boldsymbol{u}_b = (u_{b,1}(x_1, x_2), u_{b,2}(x_1, x_2), 0)^{\mathrm{T}}$. For these flows homogeneous steady solutions are also steady under stratification. Thus, the effects of stratification are easily extracted by changing only the Froude number $F_h$, while the base flow is unchanged.

We integrate (2.13)–(2.17) by the fourth-order Runge–Kutta method. Given the strength of stratification by the Froude number $F_h$, the initial conditions should be specified to have particular solutions. Among the initial conditions, one parameter, which is denoted by $\beta$ in the following sections, is required for $\boldsymbol{x}(0)$ to identify a periodic orbit in a two-dimensional flow; the actual definition of $\beta$ is shown for each flow in the following sections. Another parameter is required for $\boldsymbol{k}(0)$ to specify the direction of the wavevector which satisfies (2.18); we take the angle between $\boldsymbol{e}_3$ and $\boldsymbol{k}(0)$, which is denoted by $\theta_0$. It should be pointed out that the magnitude of $\boldsymbol{k}(0)$ is arbitrary since the right-hand side of (2.16) does not depend on the magnitude of $\boldsymbol{k}$ after taking the short-wave limit. For the amplitude $\boldsymbol{a}(0)$ and $r(0)$, three independent initial conditions satisfying (2.13) are considered; the results do not depend on the choice of the initial conditions since the space spanned by the three initial conditions is common. As a result, we obtain the (largest) growth rate $\sigma$ as a function of $\beta$, $\theta_0$ and $F_h$: $\sigma = \sigma(\beta, \theta_0, F_h)$.

### 2.3. *Useful formulation*

After solving (2.14) and (2.15), we are left with equations for the amplitude $\boldsymbol{a}$ and density $r$. Although $\boldsymbol{a}$ and $r$ have four components in total, the incompressibility condition (2.13) implies that the essential degree of freedom is three, as pointed out in the previous subsection. The number of dependent variables can be reduced as in Bayly, Holm & Lifshiftz (1996), who considered homogeneous two-dimensional base flow. Let us introduce

$$p = \frac{|\boldsymbol{k}|}{|\boldsymbol{k}_\perp|}\boldsymbol{k}_\perp \cdot \boldsymbol{a}_\perp, \quad q = \frac{|\boldsymbol{k}|}{|\boldsymbol{k}_\perp|}(\boldsymbol{k}_\perp \times \boldsymbol{a}_\perp)\cdot \boldsymbol{e}_3, \quad s = \frac{|\boldsymbol{k}|}{|\boldsymbol{k}_\perp|} r \qquad (2.21a\text{–}c)$$

as in Bayly *et al.* (1996), where $\boldsymbol{k}_\perp = (k_1, k_2)^{\mathrm{T}}$ and $\boldsymbol{a}_\perp = (a_1, a_2)^{\mathrm{T}}$. Then (2.16) and (2.17) are reduced to

$$\frac{\mathrm{d}}{\mathrm{d}t}\begin{pmatrix} p \\ q \\ s \end{pmatrix} = \begin{pmatrix} \dfrac{\mathrm{d}}{\mathrm{d}t}\log\dfrac{|\boldsymbol{k}_\perp|}{|\boldsymbol{k}|} & \dfrac{2k_3^2\mathcal{H}\boldsymbol{k}_\perp\cdot\boldsymbol{k}_\perp}{|\boldsymbol{k}|^2|\boldsymbol{k}_\perp|^2} & \dfrac{|\boldsymbol{k}_\perp|^2}{|\boldsymbol{k}|^2}k_3 \\ -W & -\dfrac{\mathrm{d}}{\mathrm{d}t}\log\dfrac{|\boldsymbol{k}_\perp|}{|\boldsymbol{k}|} & 0 \\ -\dfrac{1}{F_h^2 k_3} & 0 & -\dfrac{\mathrm{d}}{\mathrm{d}t}\log\dfrac{|\boldsymbol{k}_\perp|}{|\boldsymbol{k}|} \end{pmatrix}\begin{pmatrix} p \\ q \\ s \end{pmatrix}, \qquad (2.22)$$

where $W = \boldsymbol{L}_{12} - \boldsymbol{L}_{21}$ is the vorticity of the base flow, $\boldsymbol{L}_\perp = \left(\begin{smallmatrix} \boldsymbol{L}_{11} & \boldsymbol{L}_{12} \\ \boldsymbol{L}_{21} & \boldsymbol{L}_{22} \end{smallmatrix}\right)$, $\mathcal{H} = \boldsymbol{L}_\perp \left(\begin{smallmatrix} 0 & 1 \\ -1 & 0 \end{smallmatrix}\right)$ and $\boldsymbol{L} = \left(\begin{smallmatrix} \boldsymbol{L}_\perp & \boldsymbol{0} \\ \boldsymbol{0}^{\mathrm{T}} & 0 \end{smallmatrix}\right)$. We can further derive

$$\frac{\mathrm{d}^2 p}{\mathrm{d}t^2} = V_p\, p + C_q q + C_s s, \qquad (2.23)$$

where

$$V_p = \left(\frac{\mathrm{d}}{\mathrm{d}t}\log\frac{|\boldsymbol{k}_\perp|}{|\boldsymbol{k}|}\right)^2 + \frac{\mathrm{d}^2}{\mathrm{d}t^2}\log\frac{|\boldsymbol{k}_\perp|}{|\boldsymbol{k}|} - \frac{2Wk_3^2\mathcal{H}\boldsymbol{k}_\perp\cdot\boldsymbol{k}_\perp}{|\boldsymbol{k}|^2|\boldsymbol{k}_\perp|^2} - \frac{|\boldsymbol{k}_\perp|^2}{F_h^2|\boldsymbol{k}|^2}, \qquad (2.24)$$

$$C_q = \frac{\mathrm{d}}{\mathrm{d}t}\left(\frac{2k_3^2\mathcal{H}\boldsymbol{k}_\perp\cdot\boldsymbol{k}_\perp}{|\boldsymbol{k}|^2|\boldsymbol{k}_\perp|^2}\right), \tag{2.25}$$

$$C_s = \frac{\mathrm{d}}{\mathrm{d}t}\left(\frac{|\boldsymbol{k}_\perp|^2}{|\boldsymbol{k}|^2}k_3\right). \tag{2.26}$$

Equation (2.23) is useful and used in the next section, although it is not a closed equation as in Bayly *et al.* (1996). In stratified fluids under the Boussinesq approximation, potential vorticity is conserved along each streamline. In the present case it implies $q = F_h^2 k_3 Ws + c|\boldsymbol{k}|/|\boldsymbol{k}_\perp|$ where $c$ is a constant determined by the initial conditions. Using this relation we can derive a closed equation for $s$ as in Aspden & Vanneste (2009); when the solution grows exponentially we can neglect the second term $c|\boldsymbol{k}|/|\boldsymbol{k}_\perp| \ll |F_h^2 k_3 Ws|$, which leads to

$$\frac{\mathrm{d}^2 s}{\mathrm{d}t^2} = V_s s, \tag{2.27}$$

where

$$V_s = \left(\frac{\mathrm{d}}{\mathrm{d}t}\log\frac{|\boldsymbol{k}_\perp|}{|\boldsymbol{k}|}\right)^2 - \frac{\mathrm{d}^2}{\mathrm{d}t^2}\log\frac{|\boldsymbol{k}_\perp|}{|\boldsymbol{k}|} - \frac{2Wk_3^2\mathcal{H}\boldsymbol{k}_\perp\cdot\boldsymbol{k}_\perp}{|\boldsymbol{k}|^2|\boldsymbol{k}_\perp|^2} - \frac{|\boldsymbol{k}_\perp|^2}{F_h^2|\boldsymbol{k}|^2}. \tag{2.28}$$

## 3. Stability of stratified 2-D Taylor–Green vortices

In this section we study the local stability of stratified 2-D Taylor–Green vortices in detail. It is shown that there exists a new instability for which the mechanism is revealed using a simple model. The stability of homogeneous 2-D Taylor–Green vortices has been studied by local stability analysis, modal stability analysis and non-modal analysis (Sipp & Jacquin 1998; Gau & Hattori 2014); however, there is no result for the stratified case to the authors' knowledge.

### 3.1. *Base flow and initial conditions*

The streamfunction of 2-D Taylor–Green vortices is

$$\psi = \frac{A}{{b_1}^2 + {b_2}^2}\sin(b_1 x_1)\sin(b_2 x_2), \tag{3.1}$$

where $A$ is a constant and $b_1 = 2\pi/d_1$, $b_2 = 2\pi/d_2$ with $d_1$ and $d_2$ being spatial periods in the $x_1$ and $x_2$ directions. As shown in figure 1, the streamlines are periodic orbits of fluid particles except cell boundaries $x_1 = (n_1/2)d_1$ and $x_2 = (n_2/2)d_2$, where $n_1$ and $n_2$ are integers. This flow has elliptic stagnation points at $(x_1, x_2) = ((n_1/2 + 1/4)d_1, (n_2/2 + 1/4)d_2)$ and hyperbolic stagnation points at $(x_1, x_2) = ((n_1/2)d_1, (n_2/2)d_2)$. The strain rates at an elliptic stagnation point and a hyperbolic stagnation point normalized by the maximum vorticity $A$ are

$$\varepsilon_e = \frac{|{b_1}^2 - {b_2}^2|}{2({b_1}^2 + {b_2}^2)}, \quad \varepsilon_h = \frac{b_1 b_2}{{b_1}^2 + {b_2}^2}, \tag{3.2a,b}$$

respectively. Thus, both the elliptic instability and hyperbolic instability can occur in general. The flow has several symmetries: translations $(x_1, x_2; \psi) \to (x_1 + n_1 d_1, x_2 + n_2 d_2; \psi)$, $(x_1, x_2; \psi) \to (x_1 + d_1/2, x_2; -\psi)$ and $(x_1, x_2; \psi) \to (x_1, x_2 + d_2/2; -\psi)$,

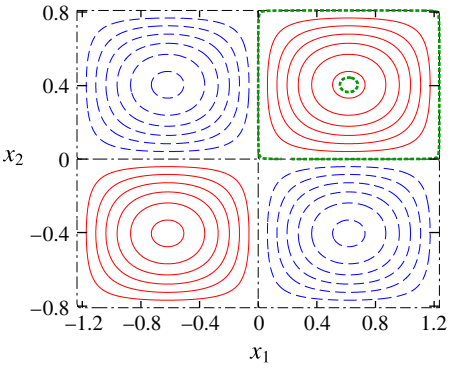


FIGURE 1. (Colour online) Streamlines of two-dimensional (2-D) Taylor–Green vortices. $\varepsilon_e = 0.2$. The solid and dashed lines correspond to positive and negative values of the streamfunction, respectively. The streamlines near the vortex centre ($\beta = 0.1$) and the boundary of the cell ($\beta = 0.999$) are marked by thick lines.

mirror reflections $(x_1, x_2; \psi) \to (-x_1, x_2; -\psi)$, $(x_1, x_2; \psi) \to (x_1, -x_2; -\psi)$, $(x_1 - d_1/4, x_2; \psi) \to (-(x_1 - d_1/4), x_2; \psi)$ and $(x_1, x_2 - d_2/4; \psi) \to (x_1, -(x_2 - d_2/4); \psi)$ and their products. Thus it suffices to investigate instability of streamlines in a single cell $[0, d_1/2] \times [0, d_2/2]$. When $d_1 = d_2$ or $\varepsilon_e = 0$, there is an additional symmetry with respect to a $\pi/2$ rotation $(x_1, x_2; \psi) \to (-x_2, x_1; -\psi)$.

We choose two values of $\varepsilon_e$: $\varepsilon_e = 0$ and 0.2; when $F_h = \infty$ (homogeneous case), the elliptic instability does not occur for the former, while it occurs for the latter. The initial conditions for the particle motion and the wavevector are

$$\boldsymbol{x}(0) = \left(\frac{d_1}{2}(1-\beta), \frac{d_2}{2}, 0\right)^{\mathrm{T}}, \quad 0 \leqslant \beta < 1 \tag{3.3}$$

$$\boldsymbol{k}(0) = (\sin\theta_0, 0, \cos\theta_0)^{\mathrm{T}}, \tag{3.4}$$

respectively. The elliptic stagnation point and the cell boundary correspond to $\beta = 0$ and 1, respectively. The length and velocity scales are chosen as $L_0 = \sqrt{d_1 d_2}/2$, the geometric mean of the side lengths of one cell, and $U_0 = AL_0/(2\pi)$, the maximum velocity when $d_1 = d_2$. The growth rate is scaled by $\sigma_0 = U_0/L_0 = A/(2\pi)$.

### 3.2. *Numerical results*

Figure 2 shows the growth rate $\sigma$ as a function of $\theta_0$ and $F_h$ on a streamline near the elliptic stagnation point $\beta = 0.1$ and that near the cell boundary $\beta = 0.999$, which are shown in figure 1; the value $\beta = 0.999$, which is rather close to the cell boundary $\beta = 1$, is chosen just to elucidate the features near the boundary, although the maximum growth rate near the boundary does not depend on $\beta$ significantly, as shown below. Let us first consider the case $\varepsilon_e = 0$ (figure 2*a*,*b*). For $\beta = 0.1$, elliptic instability does not occur as expected; there is no unstable region except the region near $\theta_0 = 0°$ and $6 \leqslant 1/F_h \leqslant 12$ with small growth rate, which can be interpreted as a remnant of unstable bands for $\beta = 0.999$ shown below. For $\beta = 0.999$, although no instability occurs for weak stratification, many unstable bands appear for $1/F_h > 2$; this is a new instability. The band structure suggests that the instability is due to resonance. The angles at which the growth rate takes a local maximum become small

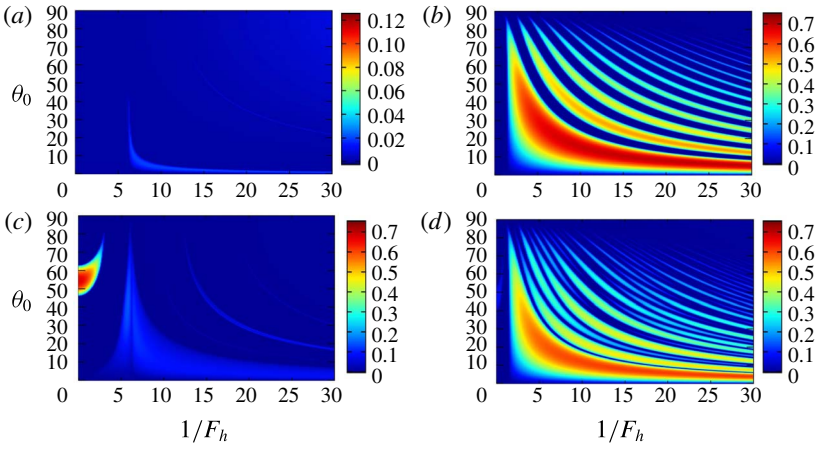


FIGURE 2. (Colour online) Growth rate $\sigma(\beta, \theta_0, F_h)$ obtained by local stability analysis. Two-dimensional Taylor–Green vortices with (*a*,*b*) $\varepsilon_e = 0$, (*c*,*d*) $\varepsilon_e = 0.2$. (*a*,*c*) Streamline near the elliptic stagnation point ($\beta = 0.1$), (*b*,*d*) streamline near the cell boundary ($\beta = 0.999$).

with $1/F_h$; it will be explained by a simplified model in § 3.3. The growth rate is large in lower bands.

For $\varepsilon_e = 0.2$ and $\beta = 0.1$ (figure 2*c*) the elliptic instability occurs; however, this region terminates at $1/F_h \approx 3.1$. This is consistent with Miyazaki & Fukumoto (1992) who showed that the elliptic instability is stabilized by stratification for an unbounded vortex. For $\beta = 0.999$, many unstable bands are again observed (figure 2*d*). The values of the growth rate are similar for $\varepsilon_e = 0$ and 0.2. Thus, the essential mechanism of the new instability would be irrelevant to the ellipticity of the vortex. However, structures of bands in figure 2(*d*) are somewhat complicated in comparison to figure 2(*b*) for $\varepsilon_e = 0$; this feature will also be explained in § 3.3.

Figure 3 shows the growth rate as a function of $\beta$ and $\theta_0$ for fixed values of $1/F_h$ for $\varepsilon_e = 0.2$. For weak stratification $1/F_h = 1$ (figure 3*a*) the unstable band of the elliptic instability stems from $(\beta, \theta_0) \approx (0, 60^\circ)$ and extends horizontally around $\theta_0 = 60^\circ$ as in the homogeneous case (Bayly 1986; Sipp & Jacquin 1998). As stratification becomes strong ($1/F_h = 2.5$, figure 3*b*) the elliptic instability becomes weak; another unstable region, which corresponds to the most unstable band in figure 2(*d*), appears near the boundary $\beta = 1$. At $1/F_h = 3.1$ (figure 3*c*) the elliptic instability is completely stabilized; the unstable region near the boundary becomes large. For strong stratification $1/F_h = 10$ (figure 3*d*) the unstable region near the boundary moves to smaller $\theta_0$ and extends to the inner region; the growth rate in this region becomes large. A few unstable bands with smaller growth rate, which correspond to the unstable bands in figure 2(*d*) appear from the boundary.

We define maximal growth rate $\sigma_{max}(\beta, F_h)$ as the maximum of the growth rate for fixed values of $\beta$ and $F_h$:

$$\sigma_{max}(\beta, F_h) = \max_{\theta_0} \sigma(\beta, \theta_0, F_h). \tag{3.5}$$

Figure 4(*a*) shows contours of $\sigma_{max}(\beta, F_h)$. The smaller region of instability, which includes $(1/F_h, \beta) = (0, 0)$, is the elliptic instability. The larger region, which is

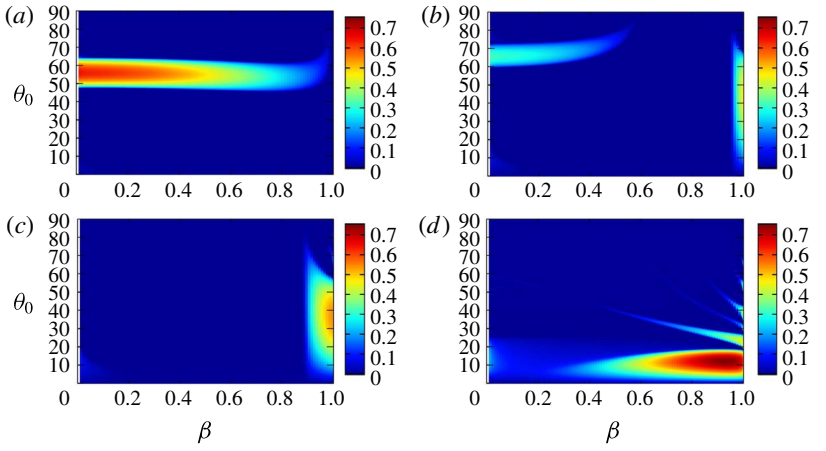


FIGURE 3. (Colour online) Growth rate $\sigma(\beta, \theta_0, F_h)$ for fixed values of $F_h$. Two-dimensional Taylor–Green vortices with $\varepsilon_e = 0.2$. (*a*) $1/F_h = 1$, (*b*) $1/F_h = 2.5$, (*c*) $1/F_h = 3.1$, (*d*) $1/F_h = 10$.

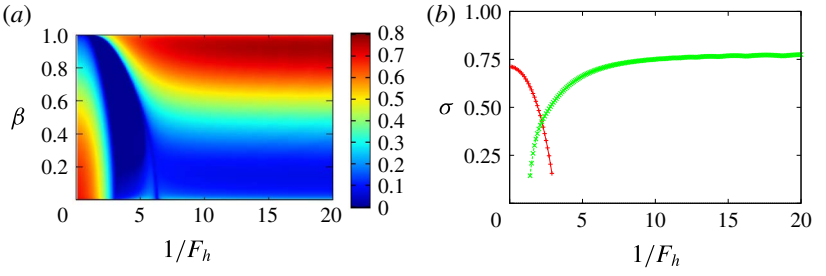


FIGURE 4. (Colour online) Maximum growth rate. Two-dimensional Taylor–Green vortices with $\varepsilon_e = 0.2$. (*a*) $\sigma_{max}(\beta, F_h) = \max_{\theta_0} \sigma(\beta, \theta_0, F_h)$, (*b*) $\sigma^*_{max}(F_h) = \max_\beta \sigma_{max}(\beta, F_h)$.

separated from the elliptic instability and extends to strong stratification, is the new instability. The growth rate of the new instability is larger than 0.5 for $\beta > 0.6$ for strong stratification; this suggests that there are corresponding eigenmodes since the region is rather broad; in fact, they are shown to exist in § 5. Figure 4(*b*) shows another maximal growth rate $\sigma^*_{max}(F_h)$ of the two instabilities, which is defined as the maximum of the growth rate for a fixed value of $F_h$:

$$\sigma^*_{max}(F_h) = \max_\beta \sigma_{max}(\beta, F_h). \tag{3.6}$$

The maximal growth rate $\sigma^*_{max}(F_h)$ of the new instability approaches a constant as $1/F_h$ increases. There is an overlap region of the two instabilities in $1 \lesssim 1/F_h \lesssim 3$, which suggests that mixed eigenmodes of the two instabilities exist.

The growth rate of the elliptic instability is $\sigma_e = (9/16)\varepsilon_e A$ in the short-wave limit (Waleffe 1990). In the present scaling it is $2\pi\sigma_e/A = 0.707$ for $\varepsilon_e = 0.2$, which is close to $\sigma = 0.711$ at $1/F_h = 0$ in figure 4(*b*). On the other hand, the growth rate of the hyperbolic instability is $\sigma_h = \varepsilon_h A$, which is $2\pi\sigma_h/A = 3.072$ in the present scaling. In figure 4(*b*) the growth rate of the new instability is $\sigma = 0.775$, which is approximately 25 % of the value above, for strong stratification. This discrepancy is not surprising:

the growth rate of the hyperbolic instability is based on the maximal value of the strain rate at the hyperbolic stagnation points; the theoretical value above is obtained only for the linear hyperbolic flow (Friedlander & Vishik 1991); in addition since there is not only a growing phase due to hyperbolic instability but also an oscillating phase in the new instability, as shown in the next subsection, the disturbance grows exponentially only in part of the time evolution.

### 3.3. *Mechanism of instability*

Here we explore the mechanism of the new instability. First it is pointed out that stratification has stabilizing effects on the local stability of the axisymmetric vortices, as shown in appendix A; in other words, the new instability does not occur in the axisymmetric vortices. It supports the importance of hyperbolic stagnation points in the new instability. Moreover, the new instability is different from the radiative instability (Le Dizès & Billant 2009) which occurs in the axisymmetric vortices in stratified fluids. In fact, by local stability analysis, which assumes the disturbances to be a localized wave packet along a streamline, the radial emission of internal waves, which is the essential mechanism of radiative instability, cannot be captured.

Next, we clarify the difference of time evolution between the homogeneous case and the stratified case focusing on the streamline near the cell boundary $\beta = 0.999$. Figure 5 shows the time evolution of the amplitude $\boldsymbol{a}$ and energy $E = |\boldsymbol{a}|^2/2$ for the homogeneous case ($1/F_h = 0$) with $\varepsilon_e = 0$. Vertical dashed lines show the instants at which the distance between the fluid particle and the nearest hyperbolic point is minimum; four successive intervals divided by the vertical dashed lines comprise one period of particle motion. Time evolutions of $a_1$ and $a_2$ are periodic with the same time period of the particle motion, while $a_3$ vanishes for $\theta_0 = 0°$. Since the orbit is close to the cell boundary for $\beta = 0.999$, each interval is close to one of the four sides of the cell. In each interval either $a_1$ or $a_2$ grows in magnitude and then decreases, while the other is nearly zero: on the bottom ($x_1 = 0 \to d_1/2$, $x_2 = 0$) $a_1 \approx 0$ and $a_2 < 0$; on the right side ($x_1 = d_1/2$, $x_2 = 0 \to d_2/2$) $a_1 < 0$ and $a_2 \approx 0$; on the top ($x_1 = d_1/2 \to 0$, $x_2 = d_2/2$) $a_1 \approx 0$ and $a_2 > 0$; and on the left side ($x_1 = 0$, $x_2 = d_2/2 \to 0$) $a_1 > 0$ and $a_2 \approx 0$. This behaviour is explained by exact solutions along the boundaries; for example, on the bottom

$$x_1 = 2\cot^{-1}(\mathrm{e}^{-At}), \quad x_2 = 0, \tag{3.7a,b}$$

$$k_1 = k_2 = 0, \quad k_3 = 1, \tag{3.8a,b}$$

$$a_1 = a_3 = 0, \quad a_2 = -\frac{1}{\cosh At}, \tag{3.9a,b}$$

is a solution to (2.13)–(2.17), where we set $d_1 = d_2 = 2\pi$ for simplicity. As evident from the solution above, exponential growth is compensated by exponential decay. However, if we start at an inner point of the cell boundaries, the solution grows exponentially as the fluid particle approaches a hyperbolic stagnation point; this is the pure hyperbolic instability (Friedlander & Vishik 1991; Sipp & Jacquin 1998). It is pointed out that the pure hyperbolic instability does not appear on the closed streamlines in the 2-D Taylor–Green vortices (Sipp & Jacquin 1998); however, it also appears as a global mode as shown in § 5.

Figure 6 shows the time evolution of the amplitude $\boldsymbol{a}$ and energy $E = (1/2)|\boldsymbol{a}|^2 + (F_h^2/2)r^2$ for a stratified case ($1/F_h = 10$). Also shown here are $p$, $q$ and $F_h s$ introduced in § 2.3. The angle $\theta_0$ is set to the most unstable case. Note that the amplitude $\boldsymbol{a}$, $p$,

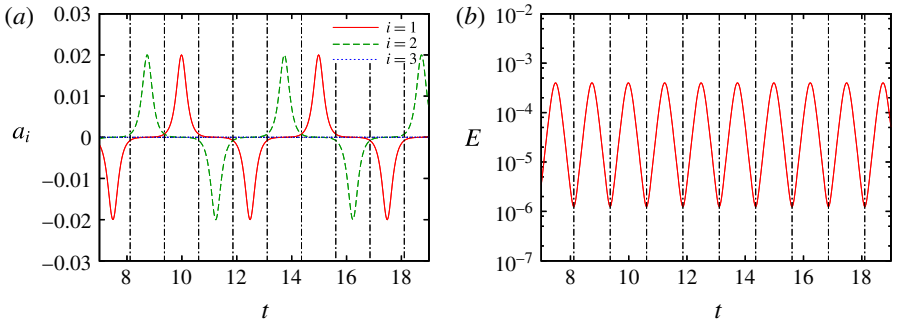


FIGURE 5. (Colour online) Time development of (*a*) $a_i$ and (*b*) energy $E$. Two-dimensional Taylor–Green vortices with $\varepsilon_e = 0$. $\beta = 0.999$, $\theta_0 = 0°$, $1/F_h = 0$. The vertical lines indicate the instants at which the fluid particle is closest to a hyperbolic stagnation point.

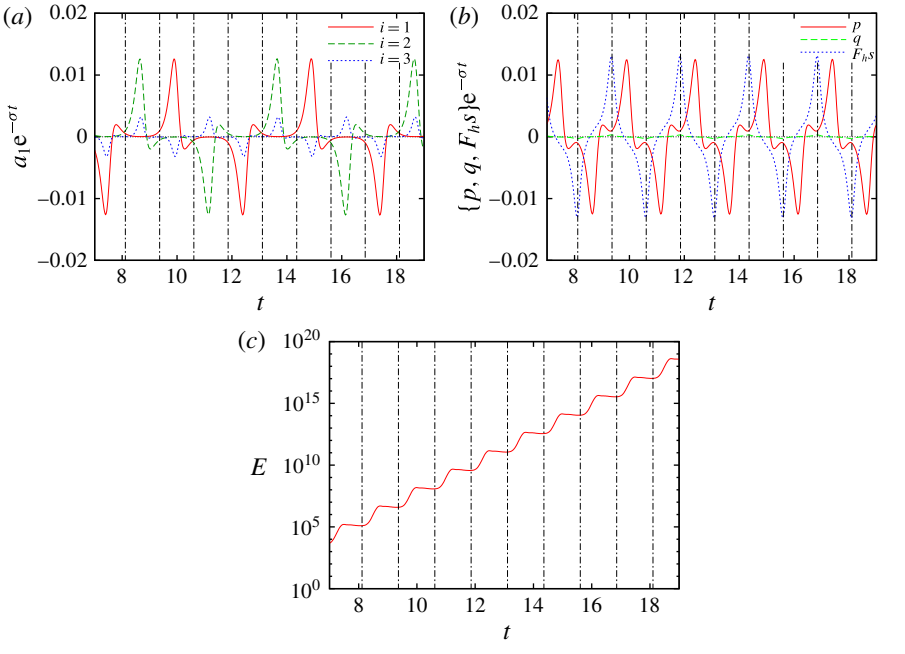


FIGURE 6. (Colour online) Time development of local disturbance. Two-dimensional Taylor–Green vortices with $\varepsilon_e = 0$. $\beta = 0.999$, $\theta_0 = 15.6°$, $1/F_h = 10$. (*a*) $a_i e^{-\sigma t}$, (*b*) $\{p, q, F_h s\}e^{-\sigma t}$, (*c*) $E$.

$q$ and $F_h s$ are multiplied by $e^{-\sigma t}$ to elucidate the oscillatory behaviour; energy grows exponentially on average with $T/4$ oscillations (figure 6*c*). Time evolutions of $e^{-\sigma t}a_1$ and $e^{-\sigma t}a_2$ look similar to the homogeneous case, but phase change is observed as smaller negative (positive) peaks of $a_i$ follow the positive (negative) peaks; it is an important difference from the homogeneous case. Although $a_3$ does not vanish, it is smaller than $a_1$ and $a_2$. In terms of $p$, $q$ and $F_h s$, $q$ is negligible (figure 6*b*). Thus we need to understand the behaviour of $p$ or $F_h s$.

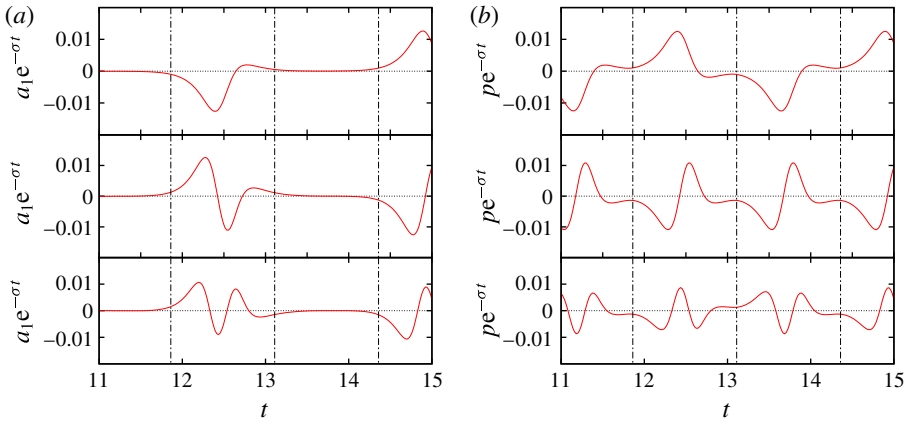


FIGURE 7. (Colour online) Time development of local disturbance. Two-dimensional Taylor–Green vortices with $\varepsilon_e = 0$. $\beta = 0.999$, $1/F_h = 10$. From top to bottom: $\theta_0 = 15.6°$, $36.0°$ and $51.8°$. (*a*) $a_1 e^{-\sigma t}$, (*b*) $pe^{-\sigma t}$.

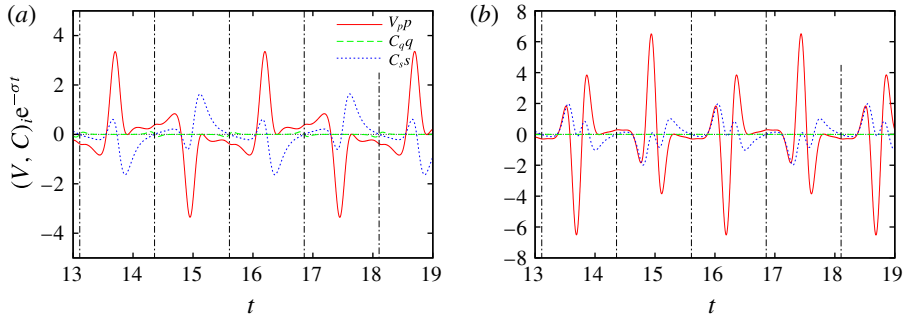


FIGURE 8. (Colour online) Comparison between three terms in (2.23) for $p$. Two-dimensional Taylor–Green vortices with $\varepsilon_e = 0$. $\beta = 0.999$, $1/F_h = 10$. (*a*) $\theta_0 = 15.6°$, (*b*) $\theta_0 = 51.8°$.

Figure 7 compares time evolution of $a_1$ and $p$ between different values of $\theta_0$; the values of $\theta_0$ are chosen as the first, second and third maximum of growth rates for $1/F_h = 10$. Again they are multiplied by $e^{-\sigma t}$ to compensate the exponential growth. It is observed that the number of oscillations increases with $\theta_0$. This supports that the instability is due to resonance and there is phase advancement by waves.

We resort to (2.23) to explore the mechanism of the instability. The reason why we prefer this equation for $p$ to the closed equation for $s$ (2.27) is that it gives us a much simpler physical interpretation. Figure 8 compares the three terms in (2.23); the first ($\theta_0 = 15.6°$) and third ($\theta_0 = 51.8°$) resonances are shown. This figure shows that $V_p p$ is the dominant term and $C_q q$ is negligible; $C_s s$ is smaller than $V_p p$ but has some contribution for $\theta_0 = 15.6°$, while it is less important for $\theta_0 = 51.8°$. Therefore, the essential mechanism of the instability may be pursued by keeping only $V_p p$, although we should keep in mind that this approximation is not so accurate for small $\theta_0$.

Figure 9 shows time evolutions of $V_p$ and $V_s$ evaluated numerically, compared for the first four resonant angles $\theta_0$ for $\varepsilon_e = 0$ and 0.2. It is observed that $V_p$ is positive near the hyperbolic stagnation points shown by the vertical dashed lines;

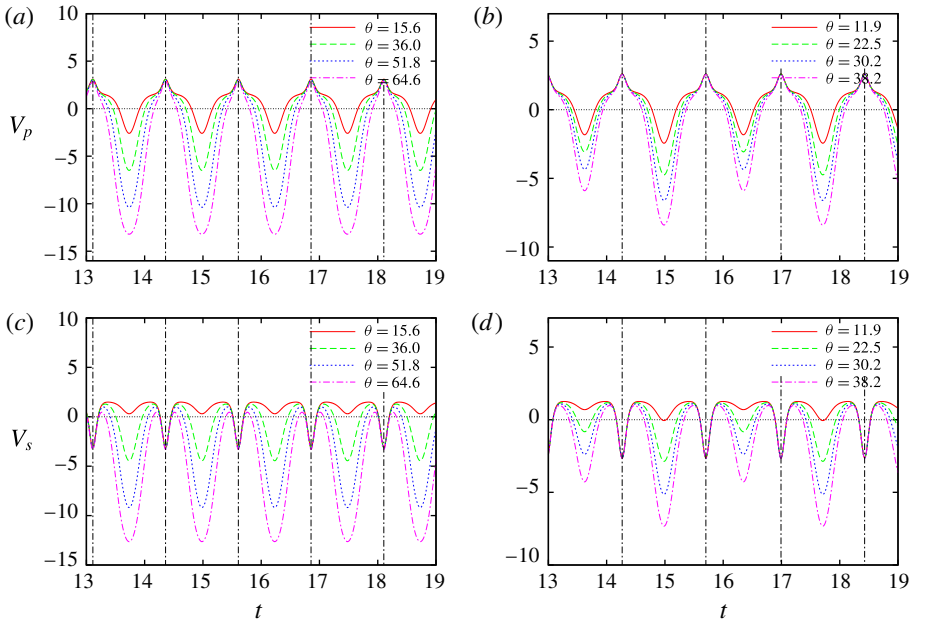


FIGURE 9. (Colour online) Time development of (*a*,*b*) $V_p$ and (*c*,*d*) $V_s$. Two-dimensional Taylor–Green vortices with (*a*,*c*) $\varepsilon_e = 0$ and (*b*,*d*) $\varepsilon_e = 0.2$. $\beta = 0.999$, $1/F_h = 10$.

this corresponds to the growing phase. On the other hand, $V_p$ is negative away from the hyperbolic stagnation points; this corresponds to the oscillation phase. The negative regions extend for higher resonance (large $\theta_0$) with the negative values of $V_p$ increasing in magnitude. While the time period of $V_p$ is $T/4$ for $\varepsilon_e = 0$ (figure 9*a*), it is $T/2$ for $\varepsilon_e = 0.2$ as two different values of the local minima of $V_p$ are repeated in turn owing to the loss of symmetry with respect to $\pi/2$ rotation; in contrast, the local maxima of $V_p$ nearly coincide with each other and do not depend significantly on $\theta_0$. The time evolutions of $V_s$ are similar to that of $V_p$ in the oscillation phase of $p$. In the growing phase, however, they are quite different; $V_s$ becomes negative near the hyperbolic stagnation points.

Figure 9 suggests that, as shown in figure 10, the time evolution of $V_p$ can be decomposed into a growth/decay phase where $V_p > 0$ (denoted by '$g/d$') and an oscillation phase where $V_p < 0$ (denoted by '$o$'), which are divided by the vertical lines. Then it would be legitimate to consider a simplified model for $V_p$ and time evolution of $p$:

$$\frac{\mathrm{d}^2 p}{\mathrm{d}t^2} = V(t)p, \tag{3.10}$$

$$V(t) = \begin{cases} -\omega_a^2 & T_m < t < t_{m1} = T_m + T_a, \\ \sigma^2 & t_{m1} < t < t_{m2} = t_{m1} + T_\sigma, \\ -\omega_b^2 & t_{m2} < t < t_{m3} = t_{m2} + T_b, \\ \sigma^2 & t_{m3} < t < T_{m+1} = t_{m3} + T_\sigma, \end{cases} \tag{3.11}$$

where $T_m = (m/2)T$ and $T/2 = T_a + T_b + 2T_\sigma$, in order to investigate the essential mechanism of the new instability. It is worth noting that (3.10) with time $t$ replaced

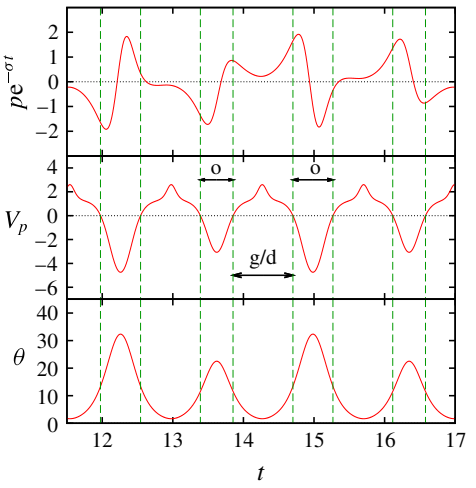


FIGURE 10. (Colour online) Decomposition into growth/decay phase (denoted by 'g/d') and oscillation phase (denoted by 'o') of $p$. Two-dimensional Taylor–Green vortices with $\varepsilon_e = 0.2$. Time evolutions of $pe^{-\sigma t}$, $V_p$ and $\theta$. $\beta = 0.999$, $\theta_0 = 30.2°$, $1/F_h = 10$.

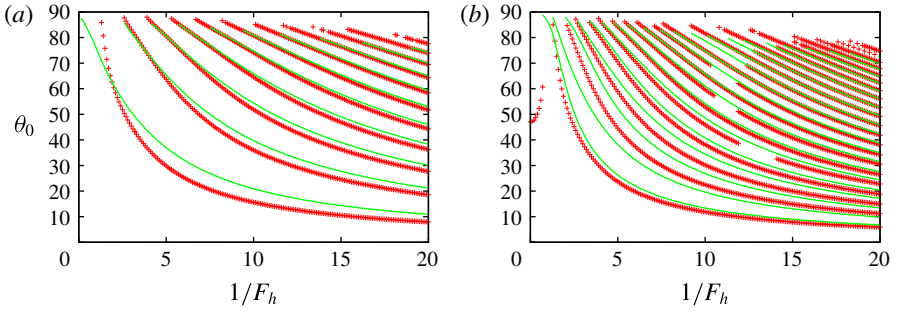


FIGURE 11. (Colour online) Resonant angle. Two-dimensional Taylor–Green vortices. The symbols show the numerical results showing extrema of the growth rate, while the solid lines show the results obtained by the simplified model (3.10) (extrema of tr $\boldsymbol{M}$). (*a*) $\varepsilon_e = 0$, $\beta = 0.999$, (*b*) $\varepsilon_e = 0.2$, $\beta = 0.999$.

by a coordinate $x$ is similar to the Kronig–Penney model for a particle in a one-dimensional lattice in quantum mechanics (Kittel 2005). Instability of solutions to (3.10) corresponds to a band gap in the Kronig–Penney model. It is pointed out that the angle $\theta = \sin^{-1} |\boldsymbol{k}_\perp|/|\boldsymbol{k}|$ is small and approaches zero near the hyperbolic stagnation points in the growth/decay phase; in fact, the initial angle $\theta_0$ at $x_2 = d_2/4$ is a local maximum of $\theta$.

It is straightforward to solve (3.10) and thereby investigate stability of the solution (see appendix B). Figure 11 compares the resonant angles between the local stability analysis and the model (3.10) for $\beta = 0.999$ and $\varepsilon_e = 0$ and 0.2. The stability and the growth rate are determined by the trace of the matrix $\boldsymbol{M}$ defined in appendix B. The local extrema of tr $\boldsymbol{M}$ are plotted for the model. The values of $\omega_a$, $\omega_b$ and $\sigma$ in (3.11) are obtained by taking the average of $V_p$ in each interval shown in figure 10. Good agreement is observed, especially for higher resonance; this is because the approximation is expected to be good for higher resonance as $C_s s$ becomes relatively

smaller than $V_p p$. The number of lines for $\varepsilon_e = 0.2$ is nearly doubled in comparison to $\varepsilon_e = 0$. This is due to break of symmetry as predicted by the model. For some higher resonances, the resonant angles are missing in the local stability analysis since the growth rate becomes small for a certain range of $F_h$ as seen in figure 2(*d*).

The above results motivate us to seek a more simplified approximation for the resonant angles. Assuming $\mathrm{e}^{2\sigma T_\sigma} \gg 1$, $\sigma \sim \omega_a$ and $\sigma \sim \omega_b$, $\mathrm{tr}\,\boldsymbol{M}$ can be approximated as

$$\begin{aligned} \mathrm{tr}\,\boldsymbol{M} &\approx \mathrm{e}^{2\sigma T_\sigma} \cos(-\omega_a T_a) \cos(-\omega_b T_b) \\ &= \tfrac{1}{2}\mathrm{e}^{2\sigma T_\sigma} [\cos(-\omega_a T_a - \omega_b T_b) + \cos(-\omega_a T_a + \omega_b T_b)]. \end{aligned} \tag{3.12}$$

For $\varepsilon_e = 0$, by noting $\omega_a = \omega_b$ and $T_a = T_b$ the above expression reduces to

$$\mathrm{tr}\,\boldsymbol{M} = \tfrac{1}{2}\mathrm{e}^{2\sigma T_\sigma}(1 + \cos 2\omega_a T_a), \tag{3.13}$$

which implies that $|\mathrm{tr}\,\boldsymbol{M}|$ takes a local maximum when

$$\omega_a T_a = m\pi, \tag{3.14}$$

but instability does not occur when $\omega_a T_a = (m + 1/2)\pi$ since $\mathrm{tr}\,\boldsymbol{M} = 0$. For $\varepsilon_e \neq 0$, on the other hand, since $-\omega_a T_a + \omega_b T_b$ varies slowly, $|\mathrm{tr}\,\boldsymbol{M}|$ takes a local maximum not only when

$$\tfrac{1}{2}(\omega_a T_a + \omega_b T_b) = m\pi, \tag{3.15}$$

but also when

$$\tfrac{1}{2}(\omega_a T_a + \omega_b T_b) = \left(m + \tfrac{1}{2}\right)\pi, \tag{3.16}$$

for which $\mathrm{tr}\,\boldsymbol{M} \approx (1/2)\mathrm{e}^{2\sigma T_\sigma}[-1 + \cos(-\omega_a T_a + \omega_b T_b)]$ can be smaller than $-2$ owing to the factor $\mathrm{e}^{2\sigma T_\sigma} \gg 1$. Thus the symmetry breaking increases the number of unstable bands as observed in figure 2(*d*). Moreover, the difference between $\omega_a T_a$ and $\omega_b T_b$ controls the magnitude of $\mathrm{tr}\,\boldsymbol{M}$, sometimes making it smaller than 2 to kill the instability as shown in figure 11(*b*).

For large $1/F_h$ the potential $V_p$ in the oscillation phase can be approximated retaining the last term

$$V_p \approx -\frac{1}{F_h^2}\sin^2\theta. \tag{3.17}$$

Thus the sum of $\omega_a T_a$ and $\omega_b T_b$ is evaluated as

$$\begin{aligned} \omega_a T_a + \omega_b T_b &\approx \int_{T_m}^{t_{m1}} \sqrt{-V_p}\,\mathrm{d}t + \int_{t_{m2}}^{t_{m3}} \sqrt{-V_p}\,\mathrm{d}t \\ &\approx \frac{1}{F_h}\int_{T_m}^{T_{m+1}} \sin\theta\,\mathrm{d}t, \end{aligned} \tag{3.18}$$

since $\theta \approx 0$ in the growth/decay phase (figure 10). Then the above resonance conditions (3.14) and (3.15) are reduced to

$$\frac{1}{F_h}\int_{T_m}^{T_{m+1}} \sin\theta\,\mathrm{d}t = 2m\pi, \tag{3.19}$$

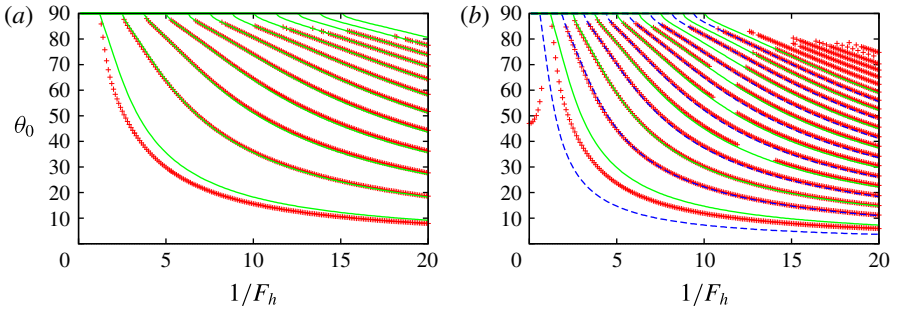


FIGURE 12. (Colour online) Resonant angle. Two-dimensional Taylor–Green vortices. The symbols are the same as in figure 11, while the solid lines and the dashed lines show (3.19) and (3.20), respectively. (*a*) $\varepsilon_e = 0$, $\beta = 0.999$, (*b*) $\varepsilon_e = 0.2$, $\beta = 0.999$.

while (3.16) is reduced to

$$\frac{1}{F_h}\int_{T_m}^{T_{m+1}} \sin\theta \, \mathrm{d}t = (2m+1)\pi. \tag{3.20}$$

Figure 12 compares the resonant angles between the local stability analysis and the simplified conditions. For $\varepsilon_e = 0.2$, solid lines and dashed lines correspond to (3.19) and (3.20), respectively. Good agreement is observed. Therefore, both the model (3.10) and the simplified conditions (3.19) and (3.20) give good approximations for the resonance condition.

To summarize, the results above establish that the new instability is due to successive hyperbolic instability near the hyperbolic stagnation points connected by a phase shift due to the internal gravity waves. We name this new instability the strato-hyperbolic instability.

## 4. Stability of other stratified vortices

In this section two stratified vortices that possess hyperbolic stagnation points are considered to investigate universality of the strato-hyperbolic instability: the Stuart vortices and the Lamb–Chaplygin dipole.

### 4.1. *Stuart vortices*

The streamfunction of the Stuart vortices is

$$\psi = \log\left(C\cosh x_2 + \sqrt{C^2-1}\cos x_1\right), \tag{4.1}$$

where $C \geqslant 1$ is a constant. As shown in figure 13(*a*), there are elliptic stagnation points at $(x_1, x_2) = ((2n+1)\pi, 0)$ and hyperbolic stagnation points at $(x_1, x_2) = (2n\pi, 0)$. The streamlines are closed inside the heteroclinic streamlines connecting the hyperbolic stagnation points shown by the dot-dashed lines. In this case, however, the motion of a fluid particle is also periodic with modulo $2\pi$ in the $x_1$ direction outside the heteroclinic streamlines. Thus we consider not only the closed streamlines but also the open streamlines outside the heteroclinic streamlines. The Stuart vortices are less symmetric than the 2-D Taylor–Green vortices: they are symmetric to translation

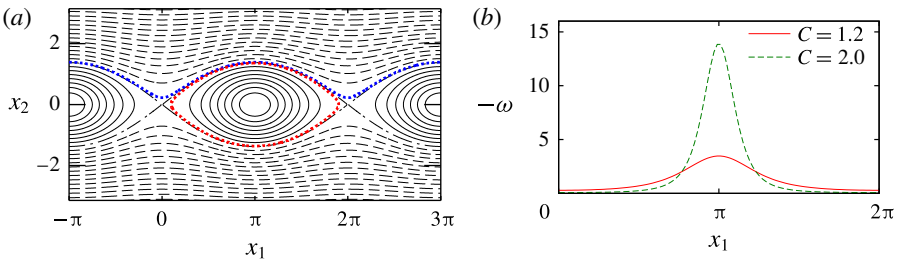


FIGURE 13. (Colour online) Stuart vortices. (*a*) Streamlines. $C = 1.2$. The thick dotted lines indicate the closed streamline with $\beta = 0.99$ and the open streamline with $\beta = 1.01$. (*b*) Vorticity distribution on $x_2 = 0$. Solid line, $C = 1.2$; dashed line, $C = 2.0$.

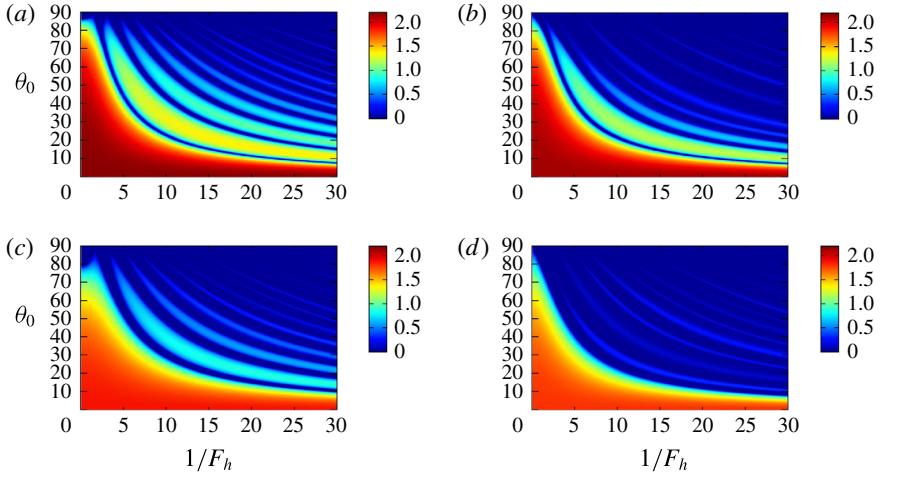


FIGURE 14. (Colour online) Growth rate $\sigma(\beta, \theta_0, F_h)$ for a closed ($\beta = 0.99$) and an open streamline ($\beta = 1.01$) near the boundary. Stuart vortices. (*a*) $C = 1.2$, $\beta = 0.99$, (*b*) $C = 1.2$, $\beta = 1.01$, (*c*) $C = 2.0$, $\beta = 0.99$, (*d*) $C = 2.0$, $\beta = 1.01$.

$(x_1, x_2; \psi) \to (x_1 + 2\pi n, x_2; \psi)$, mirror reflections $(x_1, x_2; \psi) \to (-x_1, x_2; \psi)$, $(x_1, x_2; \psi) \to (x_1, -x_2; \psi)$ and their products. The strain rates at an elliptic stagnation point and a hyperbolic stagnation point are $\varepsilon_e = \varepsilon_h = 1/2$.

We choose $C = 1.2$ and 2 in the following; vorticity is more concentrated for $C = 2$ than for $C = 1.2$ (figure 13*b*). Initial conditions are chosen as

$$\boldsymbol{x}(0) = (\pi, \beta y_c, 0)^{\mathrm{T}}, \tag{4.2}$$

$$\boldsymbol{k}(0) = (0, \sin\theta_0, \cos\theta_0)^{\mathrm{T}}, \tag{4.3}$$

where $y_c = \cosh^{-1}(1 + 2\sqrt{1 - C^{-2}})$. The closed and open streamlines correspond to $0 \leqslant \beta < 1$ and $\beta > 1$, respectively. The velocity and length scales are chosen as $U_0 = 1$, the velocity at $x_2 = \infty$ and $L_0 = 2\pi$, the spatial period in the $x_1$ direction. The growth rate is scaled by $\sigma_0 = U_0/L_0 = 1/(2\pi)$.

Figure 14 shows the growth rate as a function of $\theta_0$ and $F_h$ for a closed streamline ($\beta = 0.99$) and an open streamline ($\beta = 1.01$) near the boundary (shown in figure 13*a*). For all four cases a wide range of instability exists for the homogeneous case $1/F_h = 0$.

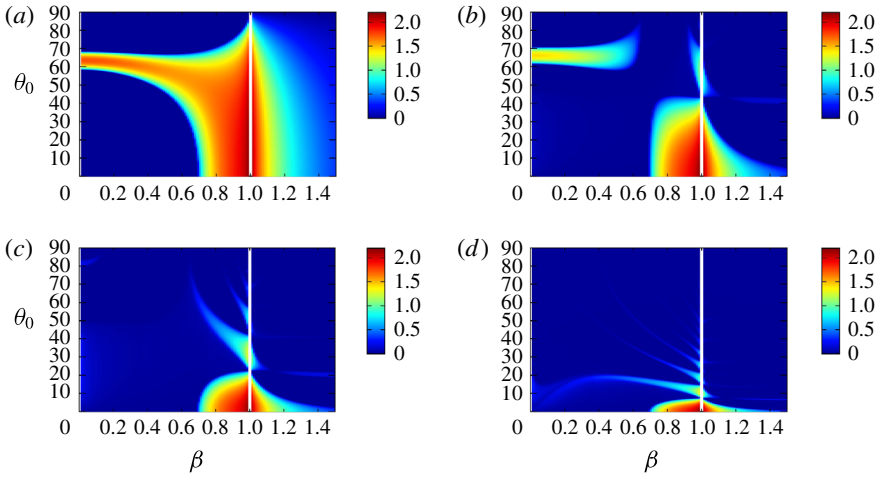


FIGURE 15. (Colour online) Growth rate $\sigma(\beta, \theta_0, F_h)$ for fixed values of $F_h$. Stuart vortices with $C = 1.2$. (*a*) $1/F_h = 0$, (*b*) $1/F_h = 5$, (*c*) $1/F_h = 10$, (*d*) $1/F_h = 30$.

This range shrinks to a small $\theta_0$ region but survives as stratification becomes strong. It forms the strongest unstable band, which is not present for the case of the 2-D Taylor–Green vortices. This strong instability is due to pure hyperbolic instability which survives in the Stuart vortices and the Lamb–Chaplygin dipole as opposed to the 2-D Taylor–Green vortices. Unstable bands similar to those observed for the 2-D Taylor–Green vortices appear for the stratified case, although they are weak for the open streamline of $C = 2$. Thus, the same mechanism as in the 2-D Taylor–Green vortices also works here.

Figure 15 shows the growth rate as a function of $\beta$ and $\theta_0$ for fixed $F_h$. We consider the case $C = 1.2$ here. In this figure both closed streamlines $0 < \beta < 1$ and open streamlines $1 < \beta < 1.5$ are considered. For the homogeneous case $1/F_h = 0$ the unstable band emanating from $(\beta, \theta_0) \approx (0, 60°)$ is due to the elliptic instability. As $\beta$ increases, this band slightly bends to small $\theta_0$ and broadens to touch $\theta_0 = 0°$ at $\beta \approx 0.7$. This behaviour has been observed for the Gaussian vortex ring (Hattori & Fukumoto 2003) and Hill's spherical vortex (Hattori & Hijiya 2010). When we consider a nearly circular vortex with weak elliptical deformation by local stability analysis, the resonance condition for the elliptic instability turns out to be

$$\cos^2\theta_0 = \left|\frac{\Omega}{2\omega}\right|, \tag{4.4}$$

where $\Omega$ is the angular velocity of the particle motion and $\omega$ is the vorticity on the streamline (Hattori & Fukumoto 2003). Thus the resonance angle becomes small as the ratio of vorticity to angular velocity decreases. If vorticity decays rapidly outside the vortex core, the right-hand side of (4.4) exceeds 1, for which there is no angle $\theta_0$ satisfying this condition. This unstable band has large growth rate near the heteroclinic streamlines $\beta = 1$ where pure hyperbolic instability for homogeneous fluid exists. It extends outside of them, but the growth rate decreases as $\beta$ further increases.

For $1/F_h = 5$, the unstable band of the elliptic instability splits into two regions: a narrow band emanating from $(\beta, \theta_0) \approx (0, 60°)$ and a region attached to $\theta_0 = 0°$. In the narrow band the growth rate is smaller than that for the homogeneous case

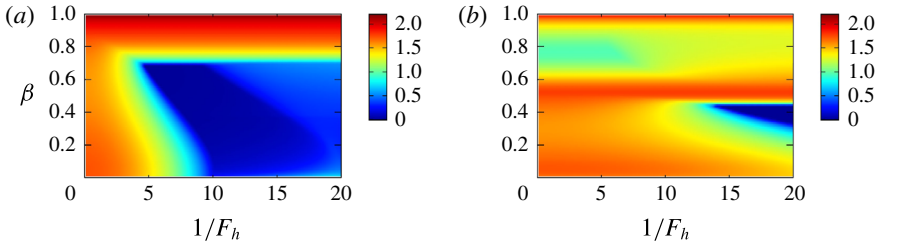


FIGURE 16. (Colour online) Maximum growth rate $\sigma_{max}(\beta, F_h)$. Stuart vortices. (*a*) $C = 1.2$, (*b*) $C = 2$.

$1/F_h = 0$; this band terminates at $\beta \approx 0.7$. The region attached to $\theta_0 = 0°$ is due to the elliptic instability and the pure hyperbolic instability. The growth rate in this region is nearly unchanged. Another weak unstable band due to the new instability appears above this region. The effects of stratification are weak for small $\theta_0$ as the term due to stratification in (2.26), $|\boldsymbol{k}_\perp|^2/(F_h^2|\boldsymbol{k}|^2) = \sin^2\theta/F_h^2$, becomes small. In particular, it can be easily confirmed that there is no effect of stratification for $\theta_0 = 0°$. Thus the region attached to $\theta_0 = 0°$ shrinks as $1/F_h$ increases, but it never disappears. For $1/F_h =$ 10 and 30 the narrow band of elliptic instability disappears. The number of unstable bands near the heteroclinic streamlines $\beta = 1$ increases with $1/F_h$.

Figure 16 shows contours of maximal growth rate $\sigma_{max}(\beta, F_h)$. The pure hyperbolic instability and the elliptic instability are dominant. For $C = 1.2$, the narrow band in figure 15 corresponds to the region $\beta < 0.7$ which terminates at $1/F_h \approx 10$ in figure 16, while the region attached to $\theta_0 = 0°$ in figure 15 corresponds to the horizontal band $\beta > 0.7$ in figure 16, where the growth rate is nearly independent of $1/F_h$ since the growth rate is maximum at $\theta_0 = 0°$. For $C = 2$, the narrow band in figure 15 survives at stronger stratification. The horizontal band has two extrema at $\beta = 0.52$ due to the elliptic instability and 1 due to the pure hyperbolic instability. For both cases, $\sigma^*_{max}(F_h)$ is constant as the maximum is located at $(\beta, \theta_0) = (1 - 0, 0°)$ for which the growth rate is unaffected by stratification.

We also compare the values of the growth rate with the theoretical values. The growth rate of the elliptic instability in the short-wave limit is $2\pi(9/16)\varepsilon_e = 1.767$ in the present scaling, which is close to $\sigma = 1.715$ at $1/F_h = 0$ in figure 15(*a*). The growth rate of the hyperbolic instability is $2\pi\sigma_h = 3.142$ in the present scaling. The growth rates of the hyperbolic instability and the maximum growth rate of the strato-hyperbolic instability for strong stratification are $\sigma = 2.184 (= \sigma^*_{max}(F_h))$ and 1.381, which are approximately 70 % and 43 % of $2\pi\sigma_h$, respectively.

### 4.2. *Lamb–Chaplygin dipole*

The streamfunction of the Lamb–Chaplygin dipole in a frame moving with it is

$$\psi = \begin{cases} -\dfrac{2U_0R_0}{\mu_1 \mathrm{J}_0(\mu_1)} \mathrm{J}_1\left(\mu_1 \dfrac{r}{R_0}\right) \sin\phi & r \leqslant R_0 \\ -U_0 r \left(1 - \dfrac{R_0^2}{r^2}\right) \sin\phi & r > R_0, \end{cases} \tag{4.5}$$

where $U_0$ is the velocity of the uniform flow at infinity or the speed of the dipole, $R_0$ is the radius of the vortical region, $\mathrm{J}_n$ denotes the Bessel functions of the

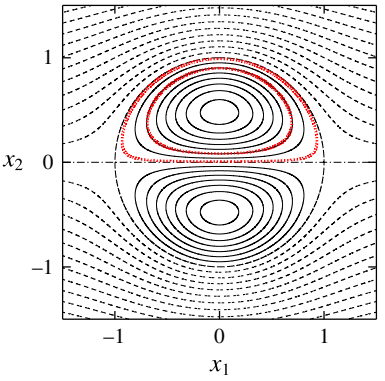


FIGURE 17. (Colour online) Streamlines of Lamb–Chaplygin dipole. The thick dotted lines indicate the streamlines with $\beta = 0.9$ and 0.99.

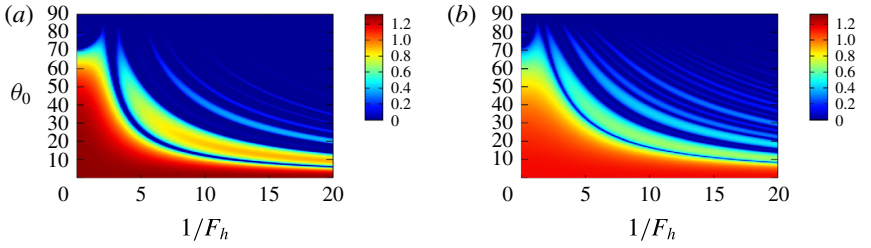


FIGURE 18. (Colour online) Growth rate $\sigma(\beta, \theta_0, F_h)$ for streamlines with (*a*) $\beta = 0.9$ and (*b*) $\beta = 0.99$. Lamb–Chaplygin dipole.

first kind, $\mu_1$ is the first zero of $J_1$ and $(r, \phi)$ is the polar coordinate system: $(x_1, x_2) = (r\cos\phi, r\sin\phi)$. As shown in figure 17, the elliptic stagnation points are located at $(x_1, x_2) = (0, \pm r_c)$, where $r_c = 0.480514R_0$, while the hyperbolic stagnation points are located at $(x_1, x_2) = (\pm R_0, 0)$. The streamlines are closed inside the circle $x_1^2 + x_2^2 = R_0^2$, which together with the segment $|x_1| < R_0, x_2 = 0$ comprises heteroclinic streamlines connecting the hyperbolic stagnation points. We focus on the upper semi-circle. It is pointed out that the base flow becomes further asymmetric as there is no symmetry with respect to translation; it is symmetric to mirror reflections $(x_1, x_2; \psi) \to (-x_1, x_2; \psi)$, $(x_1, x_2; \psi) \to (x_1, -x_2; -\psi)$. The strain rates at the elliptic stagnation points and the hyperbolic stagnation points normalized by maximum vorticity $\omega_{max} = -2\mu_1 U_0 J_1(\mu_1 r_c/R_0)/(J_0(\mu_1)R_0)$ are $\varepsilon_e = 0.2050$ and $\varepsilon_h = 0.1806$, respectively.

The initial conditions are chosen as

$$\boldsymbol{x}(0) = (0, r_c + \beta(R_0 - r_c), 0)^{\mathrm{T}}, \tag{4.6}$$

$$\boldsymbol{k}(0) = (0, \sin\theta_0, \cos\theta_0)^{\mathrm{T}}. \tag{4.7}$$

The elliptic stagnation point and the heteroclinic streamlines correspond to $\beta = 0$ and 1, respectively. In the following the velocity and the length are non-dimensionalized by $U_0$ and $R_0$, respectively. The growth rate is scaled by $\sigma_0 = U_0/R_0$.

Figure 18 shows the growth rate as a function of $\theta_0$ and $1/F_h$ for two streamlines near the heteroclinic streamlines, $\beta = 0.9$ and 0.99. It is similar to that for the Stuart

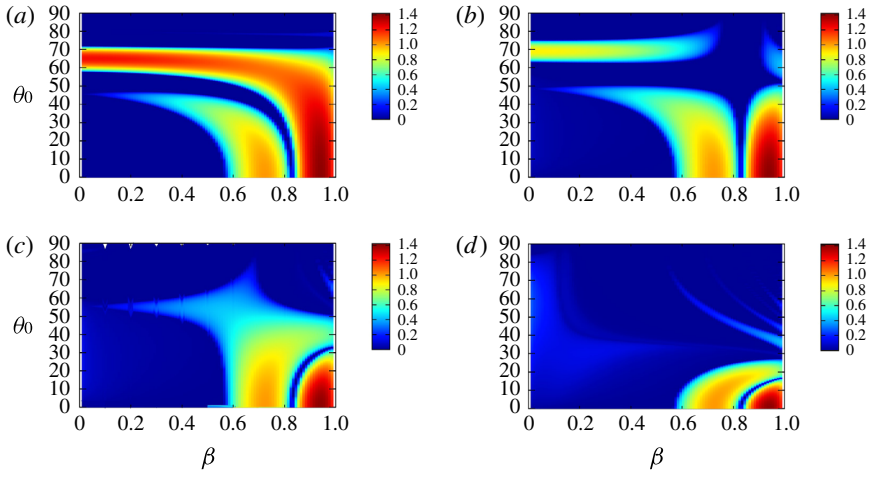


FIGURE 19. (Colour online) Growth rate $\sigma(\beta, \theta_0, F_h)$ for fixed values of $F_h$. Lamb–Chaplygin dipole. (*a*) $1/F_h = 0$, (*b*) $1/F_h = 3$, (*c*) $1/F_h = 5$, (*d*) $1/F_h = 10$.

vortices (figure 14). There is a strongly unstable region which touches $\theta_0 = 0°$; this region is due to the elliptic instability and the pure hyperbolic instability. Several unstable bands of strato-hyperbolic instability are observed above this region. The number of visible unstable bands is larger for $\beta = 0.99$, but the growth rate in the first band of strato-hyperbolic instability is larger for $\beta = 0.9$.

Figure 19 shows the growth rate as a function of $\beta$ and $\theta_0$ for four values of $1/F_h$. For the homogeneous case $1/F_h = 0$ (figure 19*a*), the elliptic instability appears as a band emanating from $(\beta, \theta_0) \approx (0, 60°)$; the band bends near $\beta = 0.8$, touches $\theta_0 = 0°$ and merges into the region of pure hyperbolic instability as in the case of the Stuart vortices (figure 15*a*). In addition there is another unstable region below the elliptic instability; this is due to the tripolar instability (Le Dizès & Eloy 1999; Eloy & Le Dizès 2001). In fact, the base flow can be expanded around the elliptic stagnation point as

$$\boldsymbol{u}_b(r, \phi) = \boldsymbol{u}_b^{(2)}(r)\mathrm{e}^{2\mathrm{i}\phi} + \boldsymbol{u}_b^{(3)}(r)\mathrm{e}^{3\mathrm{i}\phi} + \cdots, \tag{4.8}$$

where the $\mathrm{e}^{\mathrm{i}\phi}$ component, which corresponds to the uniform flow, vanishes at the stagnation point, the $\mathrm{e}^{2\mathrm{i}\phi}$ component is responsible for the elliptic instability and the $\mathrm{e}^{3\mathrm{i}\phi}$ component gives rise to the tripolar instability; note that the $\mathrm{e}^{3\mathrm{i}\phi}$ component, which is absent for the 2-D Taylor–Green vortices and the Stuart vortices, does not vanish since the base flow is asymmetric with respect to $x = r_c$. This unstable region stems from $(\beta, \theta_0) \approx (0, 45°)$, where the value of $\theta_0$ is close to the resonance condition for the tripolar instability $\cos\theta_0 = 3/4$, which gives $\theta_0 = 41.4°$, although the growth rate is small there. The region also bends and touches $\theta_0 = 0°$. The mechanism of bending is the same as in the case of the Stuart vortices. For $1/F_h = 3$ (figure 19*b*), the elliptic instability splits into two regions as in the case of the Stuart vortices (figure 15*b*): the narrow horizontal band and the region attached to $\theta_0 = 0°$, which is also due to the pure hyperbolic instability. The growth rate in the narrow band becomes small, while that in the region attached to $\theta_0 = 0°$ is not much affected. A weak band of the strato-hyperbolic instability appears near $(\beta, \theta_0) \approx (1, 60°)$. The tripolar instability is not much affected by stratification with $1/F_h = 3$. As stratification

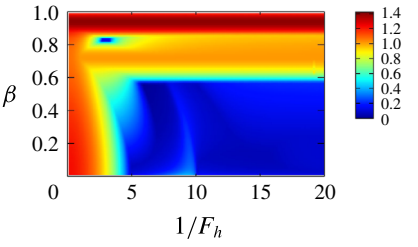


FIGURE 20. (Colour online) Maximum growth rate $\sigma_{max}(\beta, F_h)$. Lamb–Chaplygin dipole.

gets strong ($1/F_h = 5$, figure 19*c*), the narrow band of the elliptic instability disappears. The tripolar instability is somewhat stabilized for small $\beta$ or large $\theta_0$, while it now touches $\beta = 1$ and merges with the first band of strato-hyperbolic instability. For $1/F_h = 10$ (figure 19*d*), the regions of elliptic and tripolar instabilities are compressed. A few more bands of strato-hyperbolic instability with small growth rate are also observed.

Figure 20 shows contours of maximal growth rate $\sigma_{max}(\beta, F_h)$. The elliptic instability is dominant. Most of the values are due to the elliptic instability; however, the horizontal band $0.6 \lesssim \beta \lesssim 0.85$ for $1/F_h \gtrsim 5$ is due to the tripolar instability at $\theta_0 = 0°$. It is pointed out that the inner region $\beta \lesssim 0.6$ is stabilized for strong stratification, although the outer region remains unstable. The maximal growth rate $\sigma^*_{max}(F_h)$ is constant as in the case of the Stuart vortices.

The values of the growth rate are compared to the theoretical values as follows. The growth rate of the elliptic instability in the short-wave limit is $(9/16)\varepsilon_e\omega_{max}/\sigma_0 = 1.246$ in the present scaling, which is close to $\sigma = 1.221$ at $1/F_h = 0$ in figure 19(*a*). The growth rate of the hyperbolic instability is $\varepsilon_h\omega_{max}/\sigma_0 = 1.999$ in the present scaling. The growth rates of the hyperbolic instability and the maximum growth rate of the strato-hyperbolic instability for strong stratification are $\sigma = 1.405 (= \sigma^*_{max}(F_h))$ and 0.686, which are approximately 70 % and 34 % of the value above, respectively.

To summarize, the strato-hyperbolic instability appears as unstable bands also for the Stuart vortices and the Lamb–Chaplygin dipole, although the strongest instability is the elliptic instability or the pure hyperbolic instability which survives for small $\theta_0$ even in strong stratification.

## 5. Modal stability analysis

In this section, modal stability analysis of the 2-D Taylor–Green vortices in incompressible and stably stratified fluids is conducted to confirm the existence of the strato-hyperbolic instability. The growth rate and structures of the global modes of the strato-hyperbolic instability are investigated numerically to show the importance of this new instability.

### 5.1. *Numerics*

The linearized Navier–Stokes equations for incompressible and stably stratified fluids are integrated for a sufficiently long time to obtain the most unstable mode for a given set of parameters. The governing equations are the same as (2.7)–(2.9) except that a viscous term is added to (2.8):

$$\frac{\partial \boldsymbol{u}'}{\partial t} + (\boldsymbol{u}' \cdot \nabla)\boldsymbol{u}_b + (\boldsymbol{u}_b \cdot \nabla)\boldsymbol{u}' = -\nabla p' - \rho' \boldsymbol{e}_3 - \frac{1}{Re}\nabla^2 \boldsymbol{u}'. \tag{5.1}$$

These equations can be solved in the Fourier space with the terms like $(\boldsymbol{u}' \cdot \boldsymbol{\nabla})\boldsymbol{u}_b$ evaluated directly by multiplying Fourier modes since the base flow consists of only four Fourier modes.

We focus on the case $\varepsilon_e = 0$ with $L = d_x = d_y = 2\pi$ to avoid the elliptic instability. Since the base flow is independent of $x_3$, the disturbance is expanded as

$$\boldsymbol{u}' = \mathrm{e}^{\mathrm{i}k_3 x_3} \sum_{k_1=-k_{max}}^{k_{max}} \sum_{k_2=-k_{max}}^{k_{max}} \tilde{\boldsymbol{u}}_{k_1,k_2} \mathrm{e}^{\mathrm{i}(k_1 x_1 + k_2 x_2)}, \tag{5.2}$$

with a similar expression for $\rho'$; $k_{max}$ is set to 250, the number of modes being $501^2$. We start with randomized values of $\tilde{\boldsymbol{u}}_{k_1,k_2}$ at $t = 0$; then the most unstable eigenmode, if it exists, is obtained after a sufficiently long time. In addition, we also consider non-penetrating disturbances satisfying

$$\begin{bmatrix} u_1(x_1, x_2, x_3) \\ u_2(x_1, x_2, x_3) \\ u_3(x_1, x_2, x_3) \end{bmatrix} = \begin{bmatrix} -u_1(-x_1, x_2, x_3) \\ u_2(-x_1, x_2, x_3) \\ u_3(-x_1, x_2, x_3) \end{bmatrix}, \tag{5.3}$$

$$\begin{bmatrix} u_1(x_1, x_2, x_3) \\ u_2(x_1, x_2, x_3) \\ u_3(x_1, x_2, x_3) \end{bmatrix} = \begin{bmatrix} u_1(x_1, -x_2, x_3) \\ -u_2(x_1, -x_2, x_3) \\ u_3(x_1, -x_2, x_3) \end{bmatrix}, \tag{5.4}$$

which corresponds to imposing slip conditions at the cell boundaries $x_1 = n\pi$ and $x_2 = n\pi$ (Lundgren & Mansour 1996). It is pointed out that the above conditions (5.3) and (5.4) are satisfied for $t > 0$ if they are satisfied initially because of the symmetry of the base flow.

The Reynolds number based on the circulation in a single cell is $Re = 10^5$. We consider a homogeneous case and a stratified case: $1/F_h = 0$ and 5.

### 5.2. *Numerical results*

Figure 21 shows the maximal growth rate as a function of $k_3$ for homogeneous $(1/F_h = 0)$ and stratified $(1/F_h = 5)$ cases. For the homogeneous case, the growth rate is largest at $k_3 = 0$; the region $0 \leqslant k_3 \leqslant 2.4$ corresponds to the pure hyperbolic instability as strong vorticity is concentrated near the cell boundaries $x = n\pi$ and $y = n\pi$ of the vortices as shown in figure 22(*a*); this feature has been observed in Sipp & Jacquin (1998). In the region $k_3 > 2.4$ other modes corresponding to elliptic instability give the maximal growth rate; these modes exist even at $\varepsilon_e = 0$ since the strain rate does not vanish in general; in fact the elliptic instability vanishes only at the elliptic stagnation points. The mode at $k_3 = 9.2$ possesses spiral structures (figure 22*b*). However, the growth rate of these modes is smaller than that of the pure hyperbolic instability at $k_3 \approx 0$. It is pointed out that there is no unstable non-penetrating mode in the homogeneous case; the pure hyperbolic instability for $0 \leqslant k_3 \leqslant 2.4$ is oscillatory, while the mode is non-oscillatory for $k_3 > 2.4$.

For the stratified case, the pure hyperbolic instability is observed at small $k_3$; the growth rate is nearly unchanged at $k_3 \approx 0$ and the mode structures shown in figure 23(*a*) for $k_3 = 0.1$ are similar to the homogeneous case (figure 22*a*). As $k_3$ increases, however, this pure hyperbolic instability mode is surpassed by a different mode of which structures are shown in figure 23(*b*) for $k_3 = 3.2$; it is essentially due to strato-hyperbolic instability since the mode has regions of strong vorticity

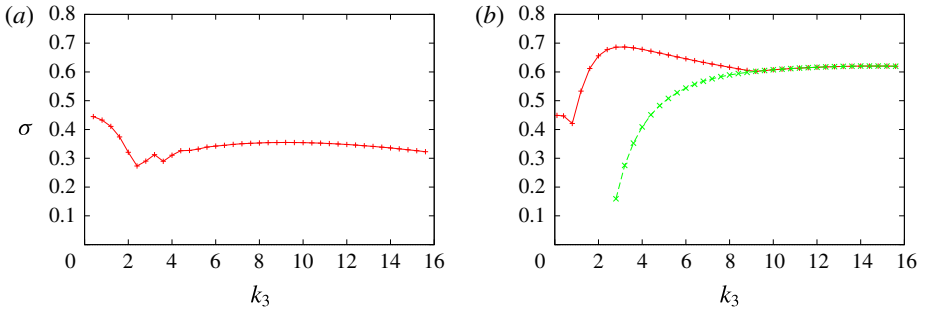


FIGURE 21. (Colour online) Growth rate obtained by modal stability analysis. The maximum growth rate for each wavenumber $k_3$. Two-dimensional Taylor–Green vortices with $\varepsilon_e = 0$ and $Re = 10^5$. The solid lines and $+$, the most unstable mode; the dashed line and $\times$, the most unstable mode satisfying slip conditions (5.3) and (5.4). (*a*) $1/F_h = 0$, (*b*) $1/F_h = 5$.

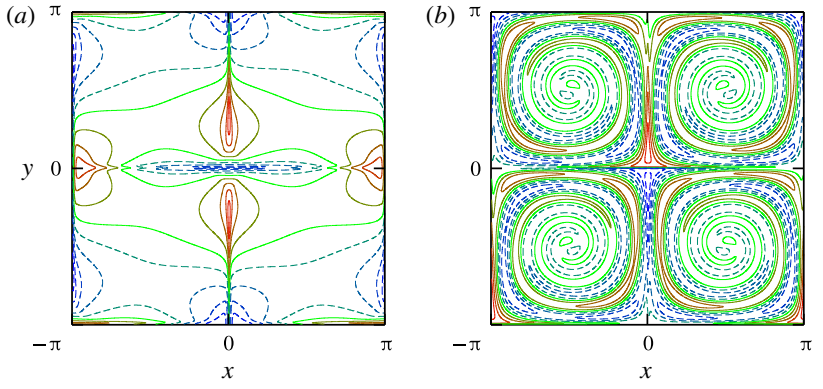


FIGURE 22. (Colour online) Unstable eigenmodes obtained by modal stability analysis. Contours of vorticity component $\omega_3$. Homogeneous 2-D Taylor–Green vortices ($1/F_h = 0$). $\varepsilon_e = 0$, $Re = 10^5$. Solid lines, $\omega_3 > 0$; dashed lines, $\omega_3 < 0$. (*a*) $k_3 = 0.1$, $(\sigma, \omega) = (0.445, 1.857)$, (*b*) $k_3 = 9.2$, $(\sigma, \omega) = (0.353, 0)$.

spread near the cell boundaries. The growth rate at $k_3 = 3.2$ is 1.7 times larger than the growth rate at $k_3 = 0.1$. As $k_3$ increases further, this mode is surpassed by the strato-hyperbolic instability mode satisfying slip conditions (5.3) and (5.4); the disturbances do not disturb the cell boundaries, quite different from the pure hyperbolic instability. These strato-hyperbolic modes are non-oscillatory, while the pure hyperbolic instability is oscillatory. Vorticity is strong near the cell boundaries as predicted by local stability analysis (figure 23*c*). The growth rate at $k_3 = 3.2$ is $\sigma = 0.687$, which is close to the value 0.775 obtained by local stability analysis in § 3.2; this also supports that the unstable modes observed at $k_3 > 0.8$ are due to the strato-hyperbolic instability.

Figure 24 shows that the structures of an unstable eigenmode are in good agreement with the results of local stability analysis. In this figure, the distributions of $p$, $q$ and $s$ defined by (2.21) on the streamline $\beta = 0.9$ of the eigenmode shown in figure 23(*c*) are compared between modal and linear stability analysis; the value $\beta = 0.9$ is chosen since the amplitude of the disturbances is nearly the largest in this case. In the

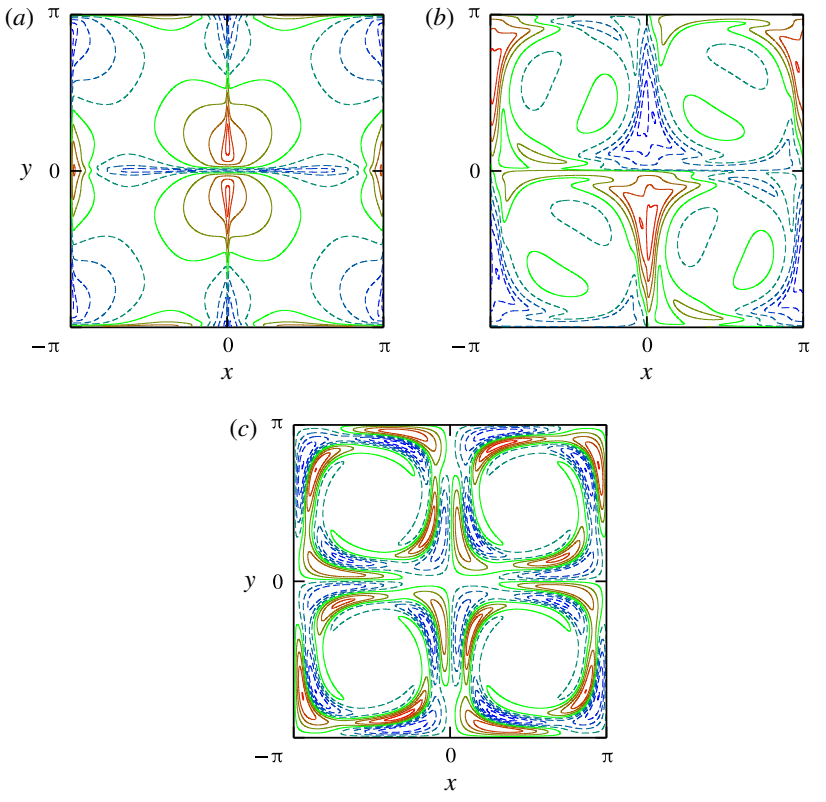


FIGURE 23. (Colour online) Unstable eigenmodes obtained by modal stability analysis. Contours of vorticity component $\omega_3$. Stratified 2-D Taylor–Green vortices ($1/F_h = 5$). $\varepsilon_e = 0$, $Re = 10^5$. Solid lines, $\omega_3 > 0$; dashed lines, $\omega_3 < 0$. (*a*) $k_3 = 0.1$, $(\sigma, \omega) = (0.449, 1.856)$, (*b*) $k_3 = 3.2$, $(\sigma, \omega) = (0.687, 0)$, (*c*) $k_3 = 14.8$, $(\sigma, \omega) = (0.620, 0)$.

modal stability analysis, the values of $p$, $q$ and $s$ are evaluated for the eigenmode along the streamline; $p \propto \boldsymbol{k}_\perp \cdot \boldsymbol{a}_\perp$ and $q \propto \boldsymbol{k}_\perp \times \boldsymbol{a}_\perp$ are calculated by horizontal divergence $\partial u_1/\partial x_1 + \partial u_2/\partial x_2$ and $\omega_3$, respectively; the horizontal axis is the time variable $\tau$ of a fluid particle which moves along the streamline and scans the values of the 'frozen' disturbance. In the local stability analysis, the time evolutions of $p$, $q$ and $s$ are multiplied by $\mathrm{e}^{-\sigma t}$ to compensate the exponential growth as in § 3.3. Since this eigenmode is not oscillatory ($\omega = 0$) and a fluid particle moves along a streamline in local stability analysis, the distributions in figures 24(*a*) and 24(*b*) can be compared directly. The phase difference and the ratio of the amplitudes of the three variables are observed to be in excellent agreement between modal and local stability analyses, confirming that the eigenmode is due to the same instability: strato-hyperbolic instability.

## 6. Concluding remarks

We have studied the stability of stably stratified vortices by local and modal stability analysis. Three base flows that possess hyperbolic stagnation points were considered: the 2-D Taylor–Green vortices, the Stuart vortices and the Lamb–Chaplygin dipole. It was shown that the elliptic instability is stabilized by stratification; it is completely

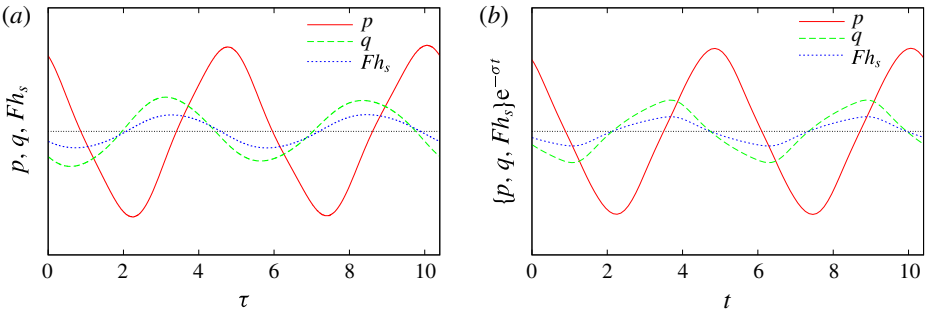


FIGURE 24. (Colour online) Comparison between modal and local stability analyses. The unstable eigenmode obtained by modal stability analysis for the stratified 2-D Taylor–Green vortices ($1/F_h = 5$). $\varepsilon_e = 0$, $Re = 10^5$, $k_3 = 14.8$ (figure 23*c*). The values of $p$, $q$ and $s$ on the streamline $\beta = 0.9$ are plotted as a function of time. (*a*) Modal stability analysis, (*b*) local stability analysis.

stabilized for the 2-D Taylor–Green vortices, while it remains and merges into the pure hyperbolic instability near the boundary or heteroclinic streamlines connecting the hyperbolic stagnation points for the Stuart vortices and the Lamb–Chaplygin dipole. The most important result is that a new instability, which we name the strato-hyperbolic instability, is found: hyperbolic instability near the hyperbolic stagnation points and phase shift by the internal gravity waves give rise to this instability. The underlying mechanism is parametric resonance as unstable band structures appear in contours of the growth rate. A simplified model explains the mechanism and the resonance curves. The growth rate of the strato-hyperbolic instability is comparable to that of the elliptic instability for the 2-D Taylor–Green vortices, while it is smaller for the Stuart vortices and the Lamb–Chaplygin dipole. For the Lamb–Chaplygin dipole, the tripolar instability was found to merge with the strato-hyperbolic instability as stratification becomes strong. The unstable eigenmodes of the strato-hyperbolic instability have been found by modal stability analysis of the 2-D Taylor–Green vortices. The structure of the eigenmode for a large wavenumber is in good agreement with the solution obtained by local stability analysis.

Although the present local stability analysis is limited to the three base flows, the strato-hyperbolic instability is expected to occur generally in stably stratified vortices that possess hyperbolic stagnation points since the underlying mechanism is a combination of hyperbolic instability and phase shift by the internal gravity waves. An important feature of the strato-hyperbolic instability is that it is strong near the heteroclinic streamlines and the core region of the vortices is rather stable. This may explain in part why a vortical structure such as the Great Red Spot on Jupiter is stable, while its outer region is turbulent; careful analysis should be done to establish this, however.

Some remarks should be given about difference from two previous results. One is the zigzag instability. Although the zigzag instability was first established analytically for the stratified Lamb–Chaplygin dipole (Billant & Chomaz 2000*b*), it is essentially a long-wave instability, although the wavelength can be short for strong stratification; it does not deform the vortex cores very much. On the other hand, the strato-hyperbolic instability is a short-wave instability as found by local stability analysis; the vertical length scale is of the same order of magnitude as the horizontal length scales. Therefore, the strato-hyperbolic instability is different from the zigzag instability.

The other relevant result is an instability found by Miyazaki & Fukumoto (1992), who considered a stratified linear flow which is unbounded and has uniform vorticity and strain. They found that the resonance between the internal gravity waves and the elliptically rotating motion gives rise to a parametric instability which they named the fundamental instability; unstable bands similar to those found in the present paper were partially observed. Unfortunately, however, the base flow is not appropriate as the expansion loses its accuracy when the fundamental instability occurs. In addition, there is no hyperbolic stagnation point in their base flow. Therefore, the strato-hyperbolic instability is also different from the fundamental instability, although they have resonance caused by the internal gravity waves in common.

One thing we should do next is to show the existence of the strato-hyperbolic modes in the Stuart vortices and the Lamb–Chaplygin dipole. We have shown that for the 2-D Taylor–Green vortices eigenmodes of the strato-hyperbolic instability concentrated near the boundary can emerge as the most unstable mode depending on the parameter values; for the Stuart vortices and the Lamb–Chaplygin dipole, they are expected to appear as the second or third most unstable mode and can be important when geometric constraint prohibits the most unstable mode. More detailed modal stability analysis is in progress and will be reported in the near future. Another future work would be to find similar types of instability caused by hyperbolic instability and phase shift by waves. For example, in magnetic fluids, the Alfvén waves can shift the phase of the disturbance to give rise to parametric instability; in rotating fluids, the dispersion relation of the inertial waves may be modified to give rise to parametric instability. These possibilities will also be pursued.

**Acknowledgements**

This work was supported by JSPS KAKENHI 17K05561. Numerical calculations were performed on the UV1000 and UV2000 at the Institute of Fluid Science, Tohoku University.

## Appendix A. Effects of stratification on the local stability of axisymmetric vortices

Here we consider the local stability of axisymmetric vortices in stably stratified vortices. The base flow is assumed to be $\boldsymbol{u}_b = U_\phi(r)\boldsymbol{e}_\phi$ in a cylindrical coordinate system $(r, \phi, z)$. Then the matrix $\boldsymbol{L}_\perp$ turns out to be

$$\boldsymbol{L}_\perp = -\frac{U_\phi}{r}\boldsymbol{e}_r\boldsymbol{e}_\phi^{\mathrm{T}} + \frac{\mathrm{d}U_\phi}{\mathrm{d}r}\boldsymbol{e}_\phi\boldsymbol{e}_r^{\mathrm{T}}. \tag{A 1}$$

By noting

$$\frac{\mathrm{d}\boldsymbol{e}_r}{\mathrm{d}t} = \frac{U_\phi}{r}\boldsymbol{e}_\phi, \quad \frac{\mathrm{d}\boldsymbol{e}_\phi}{\mathrm{d}t} = -\frac{U_\phi}{r}\boldsymbol{e}_r, \tag{A 2$a$,$b$}$$

equations (2.14) and (2.15) can be solved to give the particle motion and the wavenumber vector

$$\boldsymbol{x}(t) = r_0\boldsymbol{e}_r, \quad \boldsymbol{k}(t) = \sin\theta_0\boldsymbol{e}_r + \cos\theta_0\boldsymbol{e}_z \tag{A 3$a$,$b$}$$

(Lifschitz & Hameiri 1993; Hattori & Fukumoto 2003). Substituting the above expressions into (2.23) yields

$$\frac{\mathrm{d}^2p}{\mathrm{d}t^2} = V_p p, \quad V_p = -\frac{2WU_\phi}{r_0}\cos^2\theta_0 - \frac{1}{F_h^2}\sin^2\theta_0. \tag{A 4}$$

The solution to this equation is harmonic oscillation when $V_p < 0$, while it grows exponentially in general when $V_p > 0$. Thus Rayleigh's criterion for stability in the homogeneous case is recovered for $1/F_h = 0$: $WU_\phi = (U_\phi/r)(\mathrm{d}/\mathrm{d}r)(rU_\phi) > 0$. More importantly, stratification has stabilizing effects since $-(1/F_h^2)\sin^2\theta_0 < 0$. In particular, the axisymmetric vortices are stable when Rayleigh's criterion is satisfied according to local stability analysis.

## Appendix B. Solutions to the model equation (3.10)

Here we write down the solution to (3.10) for completeness. The solution can be expressed as

$$p = \begin{cases} A_{m1}\cos\omega_a(t-t_{m1}) + B_{m1}\sin\omega_a(t-t_{m1}) & T_m < t < t_{m1}, \\ C_{m1}\mathrm{e}^{\sigma(t-t_{m1})} + D_{m1}\mathrm{e}^{-\sigma(t-t_{m1})} & t_{m1} < t < t_{m2}, \\ A_{m2}\cos\omega_b(t-t_{m3}) + B_{m2}\sin\omega_b(t-t_{m3}) & t_{m2} < t < t_{m3}, \\ C_{m2}\mathrm{e}^{\sigma(t-t_{m3})} + D_{m2}\mathrm{e}^{-\sigma(t-t_{m3})} & t_{m3} < t < T_{m+1}, \end{cases} \tag{B 1}$$

where $A_{mi}$, $B_{mi}$, $C_{mi}$ and $D_{mi}$ are constants. At $t = T_m$ and $t_{mi}$ the values of $p$ and $\mathrm{d}p/\mathrm{d}t$ should be continuous, which gives the following matching conditions:

$$P_1 \begin{pmatrix} A_{m1} \\ B_{m1} \end{pmatrix} = Q_1 \begin{pmatrix} C_{(m-1)2} \\ D_{(m-1)2} \end{pmatrix}, \tag{B 2}$$

$$P_1 = \begin{pmatrix} \cos(-\omega_a T_a) & \sin(-\omega_a T_a) \\ -\omega_a \sin(-\omega_a T_a) & \omega_a \cos(-\omega_a T_a) \end{pmatrix}, \tag{B 3}$$

$$Q_1 = \begin{pmatrix} \mathrm{e}^{\sigma T_\sigma} & \mathrm{e}^{-\sigma T2} \\ \sigma\mathrm{e}^{\sigma T_\sigma} & -\sigma\mathrm{e}^{-\sigma T_\sigma} \end{pmatrix} \tag{B 4}$$

at $t = T_m$,

$$P_2 \begin{pmatrix} C_{m1} \\ D_{m1} \end{pmatrix} = Q_2 \begin{pmatrix} A_{m1} \\ B_{m1} \end{pmatrix}, \tag{B 5}$$

$$P_2 = \begin{pmatrix} 1 & 1 \\ \sigma & -\sigma \end{pmatrix}, \quad Q_2 = \begin{pmatrix} 1 & 0 \\ 0 & \omega_a \end{pmatrix} \tag{B 6a,b}$$

at $t = t_{m1}$,

$$P_3 \begin{pmatrix} A_{m2} \\ B_{m2} \end{pmatrix} = Q_3 \begin{pmatrix} C_{m1} \\ D_{m1} \end{pmatrix}, \tag{B 7}$$

$$P_3 = \begin{pmatrix} \cos(-\omega_b T_b) & \sin(-\omega_b T_b) \\ -\omega_b \sin(-\omega_b T_b) & \omega_b \cos(-\omega_b T_b) \end{pmatrix}, \tag{B 8}$$

$$Q_3 = \begin{pmatrix} \mathrm{e}^{\sigma T_\sigma} & \mathrm{e}^{-\sigma T_\sigma} \\ \sigma\mathrm{e}^{\sigma T_\sigma} & -\sigma\mathrm{e}^{-\sigma T_\sigma} \end{pmatrix} \tag{B 9}$$

at $t = t_{m2}$ and

$$P_4 \begin{pmatrix} C_{m2} \\ D_{m2} \end{pmatrix} = Q_4 \begin{pmatrix} A_{m2} \\ B_{m2} \end{pmatrix}, \tag{B 10}$$

$$P_4 = \begin{pmatrix} 1 & 1 \\ \sigma & -\sigma \end{pmatrix} (= P_2), \quad Q_4 = \begin{pmatrix} 1 & 0 \\ 0 & \omega_b \end{pmatrix} \tag{B 11a,b}$$

at $t = t_{m3}$. Combining the conditions above, we arrive at

$$\begin{pmatrix} C_{m2} \\ D_{m2} \end{pmatrix} = \boldsymbol{M} \begin{pmatrix} C_{(m-1)2} \\ D_{(m-1)2} \end{pmatrix}, \tag{B 12}$$

$$\boldsymbol{M} = P_4^{-1} Q_4 P_3^{-1} Q_3 P_2^{-1} Q_2 P_1^{-1} Q_1. \tag{B 13}$$

It is straightforward to confirm that $\det \boldsymbol{M} = 1$ as the equation is a Hamiltonian system. Then the stability of the solution is determined by the trace of $\boldsymbol{M}$: it is unstable and neutrally stable when $|\mathrm{tr}\, \boldsymbol{M}| > 2$ and $|\mathrm{tr}\, \boldsymbol{M}| < 2$, respectively. The trace of $\boldsymbol{M}$ is calculated as

$$\begin{aligned} \mathrm{tr}\, \boldsymbol{M} \;=\; & \mathrm{e}^{2\sigma T_\sigma} \left[ \cos(-\omega_a T_a) + \frac{1}{2} \left( -\frac{\sigma}{\omega_a} + \frac{\omega_a}{\sigma} \right) \sin(-\omega_a T_a) \right] \\ & \times \left[ \cos(-\omega_b T_b) + \frac{1}{2} \left( -\frac{\sigma}{\omega_b} + \frac{\omega_b}{\sigma} \right) \sin(-\omega_b T_b) \right] \\ & - \frac{1}{2} \left( \frac{\sigma}{\omega_a} + \frac{\omega_a}{\sigma} \right) \left( \frac{\sigma}{\omega_b} + \frac{\omega_b}{\sigma} \right) \sin(-\omega_a T_a) \sin(-\omega_b T_b) \\ & + \mathrm{e}^{-2\sigma T_\sigma} \left[ \cos(-\omega_a T_a) + \frac{1}{2} \left( \frac{\sigma}{\omega_1} - \frac{\omega_1}{\sigma} \right) \sin(-\omega_a T_a) \right] \\ & \times \left[ \cos(-\omega_b T_b) + \frac{1}{2} \left( \frac{\sigma}{\omega_b} - \frac{\omega_b}{\sigma} \right) \sin(-\omega_b T_b) \right]. \end{aligned} \tag{B 14}$$

## REFERENCES


ARRATIA, C., CAULFIELD, C. P. & CHOMAZ, J.-M. 2013 Transient perturbation growth in time-dependent mixing layers. *J. Fluid Mech.* **717**, 90–133.

ASPDEN, J. M. & VANNESTE, J. 2009 Elliptical instability of a rapidly rotating, strongly stratified fluid. *Phys. Fluids* **21**, 074104.

BAYLY, B. J. 1986 Three-dimensional instability of elliptical flow. *Phys. Rev. Lett.* **57**, 2160–2163.

BAYLY, B. J., HOLM, D. D. & LIFSCHITZ, A. 1996 Three-dimensional stability of elliptical vortex columns in external strain flows. *Phil. Trans. R. Soc. Lond.* A **354**, 895–926.

BILLANT, P. 2000 Zigzag instability of vortex pairs in stratified and rotating fluids. Part 1. General stability equations. *J. Fluid Mech.* **660**, 354–395.

BILLANT, P. & CHOMAZ, J.-M. 2000*a* Experimental evidence for a new instability of a vertical columnar vortex pair in a strongly stratified fluid. *J. Fluid Mech.* **418**, 167–188.

BILLANT, P. & CHOMAZ, J.-M. 2000*b* Theoretical analysis of the zigzag instability of a vertical columnar vortex pair in a strongly stratified fluid. *J. Fluid Mech.* **419**, 29–63.

BILLANT, P. & CHOMAZ, J.-M. 2000*c* Three-dimensional stability of a vertical columnar vortex pair in a stratified fluid. *J. Fluid Mech.* **419**, 65–91.

BILLANT, P., DELONCLE, A., CHOMAZ, J.-M. & OTHEGUY, P. 2010 Zigzag instability of vortex pairs in stratified and rotating fluids. Part 2. Analytical and numerical analyses. *J. Fluid Mech.* **660**, 396–429.

CAULFIELD, C. P. & KERSWELL, R. R. 2000 The nonlinear development of three-dimensional disturbances at hyperbolic stagnation points: a model of the braid region in mixing layers. *Phys. Fluids* **12**, 1032–1043.

CAULFIELD, C. P. & PELTIER, W. R. 2000 The anatomy of the mixing transition in homogeneous and stratified free shear layers. *J. Fluid Mech.* **413**, 1–47.

DELONCLE, A., BILLANT, P. & CHOMAZ, J.-M. 2008 Nonlinear evolution of the zigzag instability in stratified fluids: a shortcut on the route to dissipation. *J. Fluid Mech.* **599**, 229–239.

ELOY, C. & LE DIZÈS, S. 2001 Stability of the Rankine vortex in a multipolar strain field. *Phys. Fluids* **13**, 660–676.

ELOY, C., LE GAL, P. & LE DIZÈS, S. 2000 Experimental study of the multipolar vortex instability. *Phys. Rev. Lett.* **85**, 3400–3403.

FRIEDLANDER, S. & VISHIK, M. M. 1991 Instability criteria for the flow of an inviscid incompressible fluid. *Phys. Rev. Lett.* **66**, 2204–2206.

GAU, T. & HATTORI, Y. 2014 Modal and non-modal stability of two-dimensional Taylor–Green vortices. *Fluid Dyn. Res.* **46**, 031410.

GUIMBARD, D., LE DIZÈS, S., LE BARS, M., LE GAL, P. & LEBLANC, S. 2000 Elliptic instability of a stratified fluid in a rotating cylinder. *J. Fluid Mech.* **660**, 240–257.

HATTORI, Y. & FUKUMOTO, Y. 2003 Short-wavelength stability analysis of thin vortex rings. *Phys. Fluids* **15**, 3151–3163.

HATTORI, Y. & HIJIYA, K. 2010 Short-wavelength stability analysis of Hill's vortex with/without swirl. *Phys. Fluids* **22**, 074104.

ITANO, T. 2004 Stability of elliptic flow with a horizontal axis under stable stratification. *Phys. Fluids* **16**, 1164–1167.

KERSWELL, R. R. 2002 Elliptical instability. *Annu. Rev. Fluid Mech.* **34**, 83–113.

KITTEL, C. 2005 *Introduction to Solid State Physics*, 8th edn. Wiley.

LEBLANC, S. & GODEFERD, F. S. 1999 An illustration of the link between ribs and hyperbolic instability. *Phys. Fluids* **11**, 497–499.

LE DIZÈS, S. & BILLANT, P. 2009 Radiative instability in stratified vortices. *Phys. Fluids* **21**, 096602.

LE DIZÈS, S. & ELOY, C. 1999 Short-wavelength instability of a vortex in a multipolar strain field. *Phys. Fluids* **11**, 500–502.

LEWEKE, T. & WILLIAMSON, C. H. K. 1998*a* Cooperative elliptic instability of a vortex pair. *J. Fluid Mech.* **360**, 85–119.

LEWEKE, T. & WILLIAMSON, C. H. K. 1998*b* Three-dimensional instabilities in wake transition. *Eur. J. Mech. (*B*/Fluids)* **17**, 571–586.

LIFSCHITZ, A. & HAMEIRI, E. 1991 Local stability conditions in fluid dynamics. *Phys. Fluids* A **3**, 2644–2651.

LIFSCHITZ, A. & HAMEIRI, E. 1993 Localized instabilities of vortex rings with swirl. *Commun. Pure Appl. Maths* **46**, 1379–1993.

LUNDGREN, T. S. & MANSOUR, N. N. 1996 Transition to turbulence in an elliptic vortex. *J. Fluid Mech.* **307**, 43–62.

MALKUS, W. V. R. 1989 An experimental study of the global instabilities due to the tidal (elliptical) distortion of a rotating elastic cylinder. *Geophys. Astrophys. Fluid Dyn.* **48**, 123–134.

MEUNIER, P. & LEWEKE, T. 2005 Elliptic instability of a co-rotating vortex pair. *J. Fluid Mech.* **533**, 125–159.

MIYAZAKI, T. & ADACHI, K. 1998 Short-wavelength instabilities of waves in rotating stratified fluids. *Phys. Fluids* **10**, 3168–3177.

MIYAZAKI, T. & FUKUMOTO, Y. 1992 Three-dimensional instability of strained vortices in a stably stratified flow. *Phys. Fluids* A **4**, 2515–2522.

MOORE, D. W. & SAFFMAN, P. G. 1975 The instability of a straight vortex filament in a strain field. *Proc. R. Soc. Lond.* A **346**, 413–425.

OTHEGUY, P., BILLANT, P. & CHOMAZ, J.-M. 2006*a* Elliptic and zigzag instabilities on co-rotating vertical vortices in a stratified fluid. *J. Fluid Mech.* **553**, 253–272.

OTHEGUY, P., BILLANT, P. & CHOMAZ, J.-M. 2006*b* The effect of planetary rotation on the zigzag instability of co-rotating vortices in a stratified fluid. *J. Fluid Mech.* **553**, 273–281.

PIERREHUMBERT, R. T. 1986 Universal short-wave instability of two-dimensional eddies in an inviscid fluid. *Phys. Rev. Lett.* **57**, 2157–2159.

POTYLITSIN, P. G. & PELTIER, W. R. 1998 Stratification effects on the stability of columnar vortices on the $f$-plane. *J. Fluid Mech.* **355**, 45–79.

PRALITS, J. O., GIANNETTI, F. & BRANDT, L. 2013 Three-dimensional instability of the flow around a rotating circular cylinder. *J. Fluid Mech.* **730**, 5–18.

SIPP, D. & JACQUIN, L. 1998 Elliptic instability in two-dimensional flattened Taylor–Green vortices. *Phys. Fluids* **10**, 839–849.

TSAI, C.-Y. & WIDNALL, S. E. 1976 The stability of short waves on a straight vortex filament in a weak externally imposed strain field. *J. Fluid Mech.* **73**, 721–733.

WAITE, M. L. & SMOLARKIEWICZ, P. K. 2008 Instability and breakdown of a vertical vortex pair in a strongly stratified fluid. *J. Fluid Mech.* **606**, 239–273.

WALEFFE, F. 1990 On the three-dimensional instability of strained vortices. *Phys. Fluids* A **2**, 76–80.